

Analysis of Multi-epoch JWST Images of ~ 300 Little Red Dots: Tentative Detection of Variability in a Minority of Sources

ZIJIAN ZHANG ^{1,2} LINHUA JIANG ^{1,2} WEIYANG LIU ^{1,2} AND LUIS C. HO ^{1,2}

¹*Kavli Institute for Astronomy and Astrophysics, Peking University, Beijing 100871, China*

²*Department of Astronomy, School of Physics, Peking University, Beijing 100871, China*

ABSTRACT

James Webb Space Telescope (JWST) has revealed a population of red and compact sources at $z \gtrsim 5$ known as “Little Red Dots” (LRDs) that are likely active galactic nuclei (AGNs). Here we present a comprehensive study of the variability of 314 LRDs with multi-epoch JWST observations in five deep fields: UDS, GOODS-S, GOODS-N, Abell 2744, and COSMOS. Our analyses use all publicly available JWST NIRC*am* imaging data in these fields, together with multi-epoch JWST MIRI images available. We measure the significance of the variabilities (signal-to-noise ratio or SNR_{var}) for all LRDs and statistically evaluate their variabilities using the SNR_{var} distributions. We pay particular attention to the systematic offsets of photometric zero points among different epochs that seem to commonly exist. The derived SNR_{var} distributions of the LRDs, including those with broad $\text{H}\alpha/\text{H}\beta$ emission lines, follow the standard Gaussian distribution, and are generally consistent with those of the comparison samples of objects detected in the same images. This finding suggests that the LRD population on average does not show strong variability, which can be due to super-Eddington accretion of the black holes in AGNs. Alternatively, they are dominated by galaxies. We also find eight strongly variable LRD candidates with variability amplitudes of 0.24 – 0.82 mag. The rest-frame optical SEDs of these variable LRDs should have significant AGN contribution. Future JWST observations will provide more variability information of LRDs.

1. INTRODUCTION

James Webb Space Telescope is now revolutionizing our understanding of the early Universe. Among its discoveries, the identification of a class of red and compact objects has been particularly intriguing. These objects exhibit a unique “v” shape spectral energy distribution (SED) that is red in the rest-frame optical and blue in the rest-frame ultraviolet (UV). Their point-like morphology and red colors in the $\sim 2\text{--}5\ \mu\text{m}$ range (observed-frame) have earned them the name “Little Red Dots” (LRDs; e.g., [Labbé et al. 2023](#); [Barro et al. 2024](#); [Matthee et al. 2024](#)). LRDs are found to be ubiquitous from redshifts $z \sim 4$ up to $z \sim 9$ (e.g., [Barro et al. 2024](#); [Leung et al. 2023](#); [Kocevski et al. 2024](#); [Kokorev et al. 2024a](#)). Up to now, spectroscopy of more than 60 photometrically identified LRDs reveal that $\gtrsim 70\%$ of them exhibit broad Balmer lines (e.g., [Furtak et al. 2023](#); [Harikane et al. 2023](#); [Killi et al. 2023](#); [Greene et al. 2024](#); [Jani et al. 2024](#); [Matthee et al. 2024](#); [Wang et al. 2024a](#); [Williams et al. 2024](#)). Despite these observations, the true nature of LRDs remains highly debated.

The rest-frame UV-optical SEDs of these objects were initially interpreted as galaxies with high stellar masses

($\gtrsim 10^{10}\ M_{\odot}$), and their red colors are due to strong Balmer breaks or dusty star formation (e.g., [Labbé et al. 2023](#); [Akins et al. 2023](#)). JWST/MIRI observations at longer wavelength reveal a notably flat SED in the rest-frame mid-infrared (mid-IR) for several LRDs, which also suggests the presence of a $1.6\ \mu\text{m}$ stellar bump characteristic of stellar emission (e.g., [Pérez-González et al. 2024](#); [Williams et al. 2024](#)). Such galaxy-only models are further supported by the X-ray weakness of most LRDs (e.g., [Akins et al. 2024a](#); [Ananna et al. 2024](#); [Kokubo & Harikane 2024](#); [Maiolino et al. 2024](#); [Yue et al. 2024](#)), and the prominent Balmer breaks observed in several LRDs (e.g., [Baggen et al. 2024](#); [Kokorev et al. 2024b](#); [Wang et al. 2024a](#)). The inferred high masses with small effective radii ($\sim 100\ \text{pc}$) would indicate extremely high stellar mass densities (e.g., [Baggen et al. 2023](#); [Guia et al. 2024](#)), raising the possibility that the broad lines may originate from the galaxies’ kinematics.

A more natural explanation of the broad lines and compact sizes of LRDs is that they are active galactic nuclei (AGNs). [Greene et al. \(2024\)](#) explained the SED of LRDs using a scattered AGN component in the UV combined with an intrinsically reddened AGN component in the optical. Recently, [Li et al. \(2024\)](#) suggested

that LRDs can be explained by a typical AGN SED reddened by a UV-flattened extinction law similar to that seen in dense regions like the Orion Nebula or certain AGN environments. They also demonstrated that the flat mid-IR SED of LRDs may arise from an extended dust and gas distribution in the torus. In the AGN-only scenario, the observed Balmer break of some LRDs can be caused by extremely dense gas in the line of sight, and such dense gas can also naturally explain the presence of Balmer absorption features in many high-redshift AGNs (Inayoshi & Maiolino 2024). Additionally, the observed X-ray weakness of LRDs could be due to super-Eddington accretion of black holes (BHs) and does not contradict the AGN scenario (e.g., Madau & Haardt 2024; Pacucci & Narayan 2024).

Considering the co-existence of AGN and galaxy signature, many works invoke AGN-galaxy hybrid models to explain the SED of LRDs. For example, some SED fitting of the photometric SED and/or NIRSpec/PRISM data for LRDs favors a massive galaxy dominating the rest-frame UV alongside a dust-reddened AGN contributing the rest-frame optical emission (e.g., Killi et al. 2023; Ma et al. 2024; Wang et al. 2024a,b). The emission line diagnostics for an unresolved LRD by Akins et al. (2024b) also suggested that star-forming galaxy component dominates in the rest-frame UV, while AGN dominates in the rest-frame optical.

Given these ambiguous results, it becomes evident that relying solely on static SEDs/spectra may not suffice to determine the nature of LRDs, and alternative approaches are needed. One promising method is to investigate the variability of LRDs. AGNs generally exhibit distinctive variability compared with pure galaxies (e.g., Ulrich et al. 1997; Vanden Berk et al. 2004; Sesar et al. 2007), which may be related to the accretion disk instabilities (e.g., Ulrich et al. 1997). The variability amplitude of AGN depends on the wavelength, luminosity, Eddington ratio λ_{Edd} , BH mass, etc (e.g., Vanden Berk et al. 2004; MacLeod et al. 2011; Zuo et al. 2012). Assuming an Eddington ratio of 0.1, a AGN with a BH mass similar to those inferred from typical LRDs (e.g., $M_{\text{BH}} \sim 10^7 M_{\odot}$) is expected to show variability of $\gtrsim 0.1$ mag on the time scale of a few months according to the empirical model in Burke et al. (2023).

The unprecedented sensitivity of JWST has already enabled the discovery of extremely faint transient and variable sources at high redshifts (e.g., Yan et al. 2023; DeCoursey et al. 2024). Up to now, some observations in specific JWST deep fields have spanned more than two years, corresponding to approximately three months in the rest frame at $z = 7$. This time baseline is sufficient to probe the variability of low-mass AGNs, such

as LRDs. Kokubo & Harikane (2024) analyzed multi-wavelength multi-epoch NIRCcam data for 3 LRDs and two broad H α emitters in Abell 2744 field and found no significant variability. Their sample size is small, and the non-detection of variability may be due to the limited sampling of the data.

In this work, we present a systematic investigation of the variability of LRDs based on a much larger sample and complete data in five JWST deep fields: UDS, GOODS-S, GOODS-N, Abell 2744, and COSMOS. We compile all publicly available JWST/NIRCcam data and incorporate multi-epoch MIRI data for the first time. We apply careful photometric zero point offset correction and uncertainty calibration to ensure reliable results. The paper is organized as follows. In Section 2, we introduce our LRD sample. In Section 3, we describe our data and data processing, the correction of systematic photometric zero point offsets, and the calibration of photometric uncertainties. The results of the variability analyses of the whole LRD sample and several variable LRD candidates are shown in Section 4. In Section 5, we discuss the effect of the variation of the PSF and the indications of our results. Conclusions are given in Section 6. Throughout this paper, we use a cosmology with $H_0 = 67.4 \text{ km s}^{-1} \text{ Mpc}^{-1}$, $\Omega_{\text{M}} = 0.315$, and $\Omega_{\Lambda} = 0.686$ (Planck Collaboration et al. 2020). By default, measurement uncertainties are quoted at a 1σ confidence level, while upper limits are quoted at a 90% confidence level.

2. SAMPLES OF LRDs

We collected LRD samples from the literature. The main samples are from Akins et al. (2024a), Kocevski et al. (2024), and Kokorev et al. (2024a), which all present LRD samples with large sample sizes.

The LRDs in Kokorev et al. (2024a) were selected from several deep JWST/NIRCcam fields totaling $\sim 340 \text{ arcmin}^2$, including CEERS (PID1345; Bagley et al. 2023), PRIMER in COSMOS and UDS (PID1837), JADES (PID1180, 1210, 1286, 1287; Eisenstein et al. 2023a,b) and FRESCO (PID1895; Oesch et al. 2023) in GOODS-S and JEMS (PID1963; Williams et al. 2023). The sample selection of Kokorev et al. (2024a) follows the method in Labbe et al. (2023). For low redshift ($z < 6$) LRDs, they used a color cut of $F115W - F150W < 0.8$ at $1 \mu\text{m} < \lambda < 2 \mu\text{m}$ and two color cuts of $F200W - F277W > 0.7$ and $F200W - F356W > 1.0$ at $\lambda > 2 \mu\text{m}$. For higher-redshift LRDs, they used the color cuts of $F277W - F356W > 0.6$, $F277W - F444W > 0.7$, and $F150W - F200W < 0.8$. Sources were required to be spatially unresolved in F444W with $f_{\text{F444W}}(0''.4)/f_{\text{F444W}}(0''.2) < 1.7$ and removed the con-

Table 1. Number of LRDs in each field.

Field	Total sample	With multi-epoch observations	Broad-line sample
UDS	165	97	6
GOODS-S	84	70	1
GOODS-N	8	8	8
Abell 2744	29	25	15
COSMOS	520	114	1
Total number	806	314	31

tamination of brown dwarfs using F115W – F200W > –0.5 as suggested by Labbe et al. (2023).

The 341 LRDs presented in Kocevski et al. (2024) are from the CEERS, PRIMER, JADES, UNCOVER (PID2561; Bezanson et al. 2022) and NGDEEP (PID2079; Casey et al. 2023) Surveys. They selected red sources with a UV excess using an optical continuum slope cut of $\beta_{\text{opt}} > 0$ and a UV slope cut of $\beta_{\text{UV}} < -0.37$. These sources were required to be compact with a half-light radius smaller than 1.5 times that of a star in the F444W band. Furthermore, they used additional slope cuts to remove contamination from brown dwarfs ($\beta_{\text{UV}} < -2.8$) and β_{opt} boosted due to strong line emission affecting one or more bands ($\beta_{\text{F277W-F356W}} > -1$ at $z < 8$ and $\beta_{\text{F277W-F410M}} > -1$ if F410M is available). Their method can select LRDs over a wide redshift range ($z \sim 2-11$) and is less susceptible to contamination from galaxies with strong breaks.

Akins et al. (2024a) selected 434 LRDs from the 0.54 deg² COSMOS-Web Survey (PID1727; Casey et al. 2023). They selected compact sources brighter than 27.5 mag in F444W, but did not apply a blue rest-frame UV criterion, which is different from Kocevski et al. (2024) and Kokorev et al. (2024a). Instead, they focused on the red end of the spectrum with F277W – F444W > 1.5, which is a more extreme red color selection compared to other studies. This color cut biases the sample towards $z \geq 5$. Focusing on the reddest objects largely mitigates the contamination from extreme emission line galaxies. Their sample includes 37 LRDs covered by the PRIMER survey, and $\sim 90\%$ of these satisfy the multi-band color selection criteria described in Labbe et al. (2023).

We merged these three samples and removed duplicate sources based on their coordinates. Any two sources with a separation smaller than 1'' were treated as the same source. The merged sample consist of 853 different LRDs. We considered additional LRD samples from other works (Furtak et al. 2023; Harikane et al. 2023; Killi et al. 2023; Greene et al. 2024; Matthee et al.

2024; Wang et al. 2024a; Williams et al. 2024). We included eight broad H α emitters that have extended morphologies and flatter rest-frame optical SEDs than LRDs in Harikane et al. (2023) and an extended source at $z = 6.6$ (*Virgil*) detected by JWST/MIRI with photometric properties similar to those of LRDs (Iani et al. 2024),

Our final LRD sample consists of 907 LRDs in total. We give each LRD an I.D. (LID 1–907) in order of R.A. 806 LRDs are located in the UDS, GOODS-S, GOODS-N, Abell 2744, and COSMOS fields, forming a parent sample for our variability analyses. Table 1 summarizes the number of LRDs in each field. Among this sample, 31 LRDs are spectroscopically confirmed to have broad Balmer lines. We adopted their BH mass measurement in the literature (Harikane et al. 2023; Killi et al. 2023; Akins et al. 2024a; Kocevski et al. 2024; Kokorev et al. 2024b; Greene et al. 2024; Maiolino et al. 2024; Matthee et al. 2024; Wang et al. 2024a; Williams et al. 2024). In this sample, 314 LRDs have multi-epoch observations that allow us to study their variabilities. Their color-magnitude diagram (F444W v.s. F150W–F444W) and color-color diagram (F277W–F356W v.s. F277W–F444W) are shown in Figure 1. LRDs from Akins et al. (2024a) are significantly redder than those from other works, while LRDs from Kocevski et al. (2024) and Kokorev et al. (2024a) occupy larger color space.

3. DATA, PROCESSING, AND CALIBRATION

3.1. NIRC*am* Data Processing

We download raw JWST/NIRC*am* image `uncal.fits` files in the A2744, GOODS-S, GOODS-N, COSMOS, and UDS fields from the MAST archive. The detailed information of these files is summarized in Table 2. For the COSMOS field, we only reduce data in the PRIMER-COSMOS region since the other regions have few overlapping multi-epoch observations. We reduce the raw data using the combination of the *JWST Calibration Pipeline* (v.1.12.5), the CEERS NIRC*am* imaging reduction,¹ and our own custom codes. We use CRDS version 11.17.0 and CRDS context 1252. The details of the CEERS NIRC*am* imaging reduction are presented in Bagley et al. (2023). Here, we provide a brief description of the steps.

Stage 1 of the JWST Calibration Pipeline performs detector-level corrections, starting from `uncal.fits` files and ending with `rate.fits` files in units of count/s. Following the CEERS team’s scripts, before running

¹ <https://github.com/ceers/ceers-nircam>.

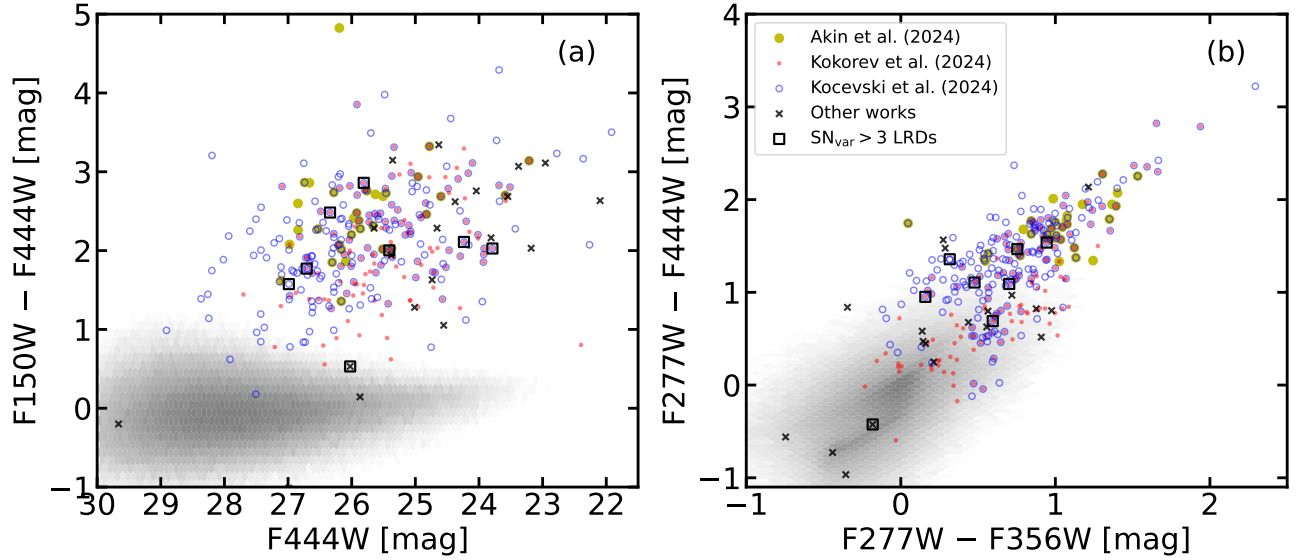


Figure 1. (a) Color-magnitude diagram of F444W vs. F150W-F444W and (b) color-color diagram of F277W-F356W vs. F277W-F444W for the 314 LRDs that have multi-epoch detections. The LRDs from Akins et al. (2024a), Kocevski et al. (2024), and Kokorev et al. (2024a) are denoted as big solid yellow dots, blue open circles, and small solid red dots, respectively. LRDs from other works are denoted as black crosses. The eight variable LRD candidates in Section 4.3 are enclosed in black squares. For comparison, all sources identified in these five fields are shown in gray.

Table 2. Information of the NIRCam images.

Field	Filters	DATE-OBS	Central R.A.	Central Decl.	PIDs
A2744	F070W F090W F115W F140M	2022-06-28	0 ^h 14 ^m 13 ^s .92	-30 ^d 25 ^m 04 ^s .80	1324 2561 2756
	F150W F162M F182M F200W	- 2023-12-10			2883 3516 3538
	F210M F250M F277W F300M				3990 4111
	F335M F356W F360M F410M				
	F430M F444W F460M F480M				
GOODS-S	F090W F115W F150W F162M	2022-09-29	3 ^h 32 ^m 35 ^s .16	-27 ^d 51 ^m 21 ^s .60	1180 1210 1283
	F182M F200W F210M F250M	- 2024-02-01			1286 1895 1963
	F277W F300M F335M F356W				2079 2198 2514
	F410M F444W				3215 3990 6541
GOODS-N	F070W F090W F115W F150W	2023-02-03	12 ^h 37 ^m 28 ^s .20	62 ^d 14 ^m 00 ^s .60	1181 1895 2514
	F182M F200W F210M F277W	- 2024-05-19			2674 3577
	F335M F356W F410M F444W				
COSMOS	F090W F115W F150W F200W	2022-11-25	10 ^h 00 ^m 30 ^s .12	2 ^d 19 ^m 48 ^s .00	1635 1727 1810
	F277W F356W F410M F444W	- 2024-05-21			1840 1933 2321
					2362 2514 3990
					6585
UDS	F090W F115W F150W F200W	2022-07-29	2 ^h 17 ^m 22 ^s .44	-5 ^d 13 ^m 19 ^s .20	1837 1840 2514
	F277W F356W F410M F444W	-2024-07-23			3990

ramp-fitting step in Stage 1 of the pipeline, we identify snowballs, increase their footprints, and flag them as `JUMP_DET` so that snowballs are better removed after the ramp-fitting step. “Wisp” features from detector B4 of the F150W, F200W, and F210M images are subtracted using the wisp templates provided by the NIR-Cam team². The $1/f$ noise, i.e., horizontal and vertical striping patterns in the images, are subtracted with `remstriping.py` in the CEERS team’s scripts.

We then run Stage 2 of the JWST Calibration Pipeline with the default parameters, which involves individual image calibrations such as flat-fielding and flux calibration. The output files are `cal.fits`. We group these files according to `DATE-OBS` in their headers, and we run Stage 3 of the JWST Calibration Pipeline to obtain a single mosaic for each `DATE-OBS` and filter in each field. Astrometry is calibrated using `TweakregStep` with `abs_refcat` set to user-provided reference catalogs in corresponding fields. For A2744, we use the UNCOVER DR2 catalog as the reference catalog (Weaver et al. 2024). For GOODS-S/GOODS-N, we generate a reference catalog as follows. We first align all LW F277W, F356W, F410M, and F444W images to detected objects in the Hubble Legacy Field GOODS-S and GOODS-N F814W image, and then combine all these LW images to make a mosaic image. We finally detect objects in the mosaic image as the reference catalog. We make reference catalog for COSMOS and UDS using the same method and their LW images are aligned to the HSC COSMOS/UDS y -band catalog (Aihara et al. 2022). After running `SkyMatchStep` and `OutlierDetectionStep`, we subtract a 2D background for each image following the method described in Bagley et al. (2023), and then run `ResampleStep` to drizzle and combine images to make one mosaic per `DATE-OBS` per filter for each field. The data for one `DATE-OBS` and one filter is defined as a *visit*. We set `pixfrac` to 0.8 and pixel scale to 0.03 arcsecond for all filters. `CRVAL` is the same for each filter, and `CRPIX` is appropriately set so that all mosaics have the same WCS grid in each field. We also combine all images to make master mosaic images for each filter in each field. Finally, a 2D background is subtracted from each mosaic using the method described in Bagley et al. (2023).

3.2. MIRI Data Processing

We also make use of all public multi-epoch JWST/MIRI F560W and F770W imaging data in the GOODS-S field, collected from PID 1180, 1207, 1283,

and 2516 (e.g., Eisenstein et al. 2023b; Rieke et al. 2024). We only consider F560W and F770W because LRDs are rarely detected in longer wavelengths, and these two bands have relatively large multi-epoch overlapping regions.

The MIRI data are reduced using v1.13.4 of the *JWST Calibration Pipeline*, with CRDS version 11.17.14 and CRDS context 1215. Our reduction pipeline is based on the public pipeline from CEERS (Yang et al. 2023),³ but we add some additional custom steps to improve the quality of the data reduction. We follow the official pipeline in Stages 1 and 2 and remove the horizontal and vertical stripes after Stage 2. As described in Alberts et al. (2024), although the default pipeline contains two levels of outlier detection, faint outliers caused by warm pixels may escape both detection steps and result in noise peaks in the resampled image. Therefore, we median stack all the `cal.fits` images after stripe removal (with pixels with DQ flag > 4 masked) and construct a warm pixels map by finding pixels that are $> 3\sigma$ above the median of all pixels of the median-stacked image. Then, we manually mask these warm pixels in all `cal.fits` images.

We also modify the super-background construction following the strategy explained in Álvarez-Márquez et al. (2023) and Alberts et al. (2024). We first construct a reliable segmentation map by iteratively running the Stage 3 and masking the sources in each `cal.fits` using the segmentation map of the mosaic image and median filtering out large gradients. A super background for a certain `cal.fits` image is then constructed by median combining all other clean `cal.fits`, with sources masked using the final segmentation map and subtracted. Then, we apply an additional 265×265 pix^2 box median subtraction to remove any remaining varying background. For the background-subtracted `cal.fits` files, we use the `TweakregStep` in Stage 3 to perform astrometry calibration with a reference catalog based on the JWST/NIRCam F444W mosaic image. Finally, the astrometry-corrected and background-subtracted `cal.fits` are processed through Stage 3, which produced both the final mosaics with a pixel scale of $0''.06$. For the MIRI data, we also produce the mosaic for each *visit* and the master mosaic for each filter.

3.3. Photometry

For the image of each *visit*, we perform aperture photometry using `SExtractor` (Bertin & Arnouts 1996) to construct its source catalog. We first smooth the images

² <https://stsci.app.box.com/s/1bymvfl1krqbdn9rnkluzqk30e8o2bne>.

³ <https://github.com/ceers/ceers-miri>.

Table 3. Relevant `SExtractor` parameters for aperture photometry in Section 3.3.

Parameter	Value
<code>PHOT_APERTURES</code>	$\max(4 \times \text{FWHM}, 5 \text{ pixels})$
<code>DETECT_MINAREA</code>	5
<code>DETECT_THRESH</code>	3
<code>ANALYSIS_THRESH</code>	3
<code>DEBLEND_NTHRESH</code>	32
<code>DEBLEND_MINCONT</code>	0.005
<code>FILTER_NAME</code>	gauss_3.0
<code>GAIN</code>	0
<code>BACK_TYPE</code>	MANUAL
<code>BACK_VALUE</code>	0
<code>BACK_SIZE</code>	100
<code>BACK_FILTERSIZE</code>	3
<code>BACKPHOTO_THICK</code>	100

with a 7×7 Gaussian kernel with an FWHM of 3 pixels to detect faint sources. To minimize the detection of spurious sources, we mask 100 pixels along the detector borders for each image, as the borders usually have fewer exposures and result in excess noise and imperfect rejection of cosmic-ray signal. We use `SExtractor` in the dual image mode, and use the master mosaic image as the detection image. The `DETECT_THRESH` parameter is set to be 3 and the `PHOT_APERTURES` parameter is set to be $4 \times \text{FWHM}$ for each band. If $4 \times \text{FWHM}$ is smaller than 5 pixels, the aperture size is set to be 5 pixels. Table 3 summarizes the `SExtractor` parameters used for photometry.

We find unusual detector artifacts in the NIRC*am* images of the COSMOS field observed on 2023-05-26 and the data of the GOODS-N field observed on 2023-05-28. These artifacts are bright and occupy large regions. They are likely caused by stray light. To address the issue of these contaminations, we mask the affected pixels using the following procedures. First, we smooth the image with a 5×5 top-hat PSF with a diameter of 5 pixels. We then run `SExtractor` with a `DETECT_THRESH` parameter of 0.2, a `DEBLEND_MINCONT` parameter of 1, and a `DETECT_MINAREA` parameter of 80,000. These parameters have been fine-tuned to reliably detect detector artifacts without detecting real sources of interest. The obtained segmentation maps are then used to mask the contamination regions. We also apply the same procedures to all other images to mask very large and bright sources.

For each *visit* pair in each common band, we match their catalogs and build a *visit*-pair catalog. We use the

astroML (Vanderplas et al. 2012) `crossmatch_angular` function to cross-match the object from one *visit* catalog to another. As the *visit* catalogs are created using the same detection image (cut-out images from the master mosaic image), the coordinates for the same sources in different *visit* catalogs should be consistent. We use a maximum distance threshold of $0''.02$ to avoid mismatch. In each *visit*-pair catalog, we calculate the magnitude difference $\Delta m = m_{\text{visit1}} - m_{\text{visit2}}$, the measured error of the magnitude difference $\Delta m_{\text{err}} = \sqrt{m_{\text{visit1, err}}^2 + m_{\text{visit2, err}}^2}$, and the mean magnitude $\langle \Delta m_{\text{err}} \rangle = (m_{\text{visit1}} + m_{\text{visit2}})/2$ for each sources. Figure 2 shows the NIRC*am* coverage and the regions of multi-epoch NIRC*am* observations for the five fields. Some LRDs are located in regions that have multi-epoch observations but still do not have multi-epoch detections since they are too faint or masked out.

We consider a source as a significantly variable source if it varied by more than $3 \times$ the combined photometric uncertainty. Before we do this, we carefully examine photometric zero points of each individual *visit* and photometric errors of sources, both of which are critical for the identification of variable sources.

3.4. Correction of Systematic Photometric Zero Point Offset

For each *visit* pair, we calculate its systematic photometric zero point offset as the median value of the iterative 3σ clipped mean Δm of sources with a `SExtractor` `FLAGS` < 1 and signal-to-noise ratio (SNR) > 5 in different magnitude bins. We verify that the offset is independent of magnitude for a certain *visit* pair. Most of the *visit* pairs show negligible offset, which confirms the photometric stability of NIRC*am* (Rigby et al. 2023). However, some *visit* pairs have large offsets of ~ 0.1 mag, which may be caused by the fluctuation of photometric zero point for different *visit* and will bias the selection of variable sources.

We correct the systematic photometric zero point offsets iteratively to achieve self-consistent results. We first select *visit* pairs with more than 50 sources to ensure the offsets are reliably calculated. The zero point offset of each *visit* is initially set as 0. For each pair, we apply the offset correction using the zero point offset difference between the two dates involved in the pair (they are all 0 in the first iteration). We then apply an iterative correction process to refine these offset correction values. In each iteration, the zero point offset of a certain *visit* is adjusted by subtracting a correction value that is computed by averaging the offsets after applying the correction across all pairs involving this *visit* date. This process is iterate for 500 times, with the offsets

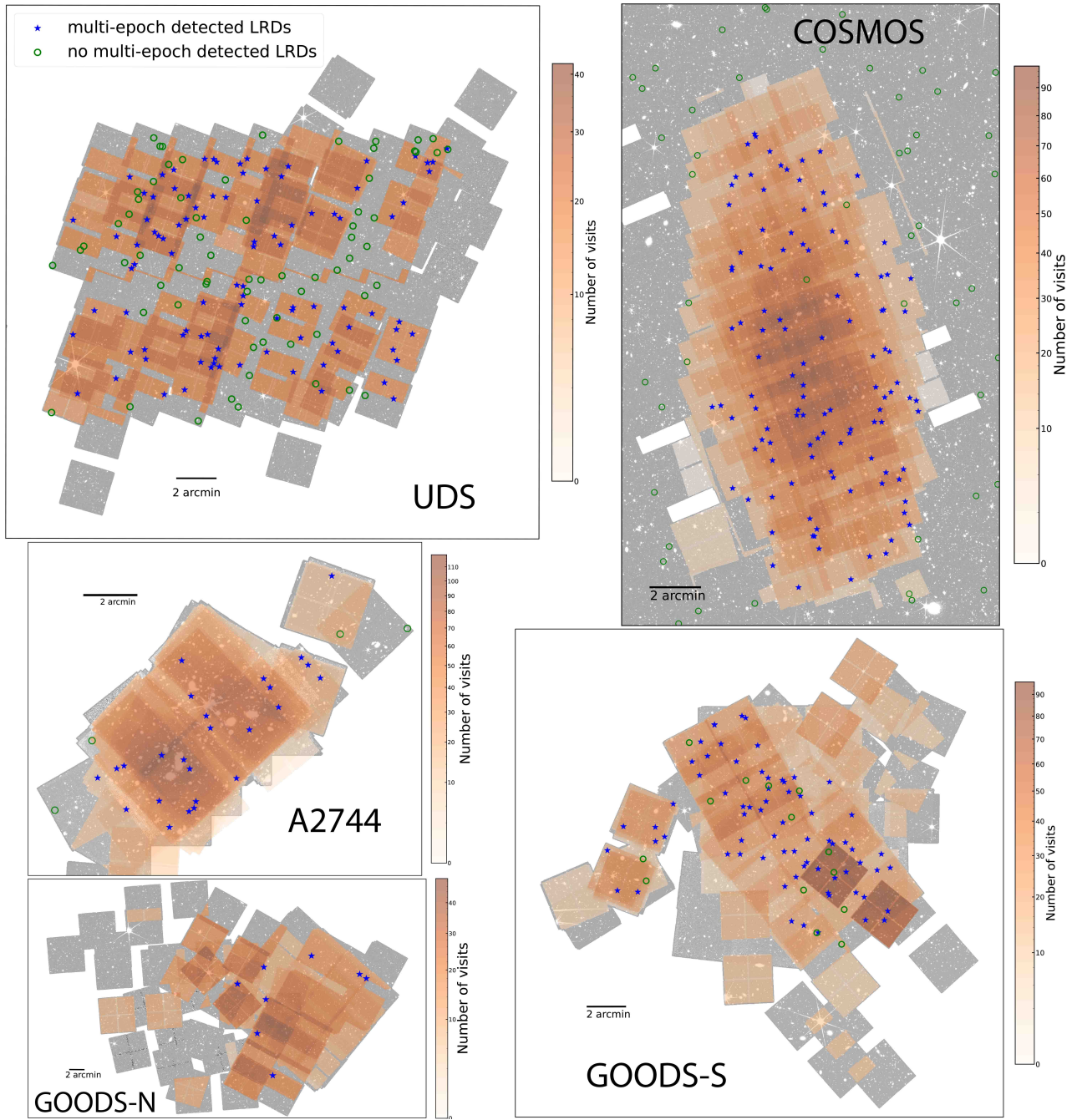


Figure 2. The full JWST/NIRCam coverage and the regions of multi-epoch NIRCam observations for UDS, A2744, GOODS-S, GOODS-N, and COSMOS fields. The background images are the co-added mosaic images of all bands in each field. Regions that have overlap between *visits* with the same band are highlighted in orange shades. A darker color indicates more *visits* with all bands combined, as shown in the color bars. All images are north up and east left. The blue stars denote the LRDs with multi-epoch detections at least in one band. The green open circles denote LRDs that do not have multi-epoch detections in any band.

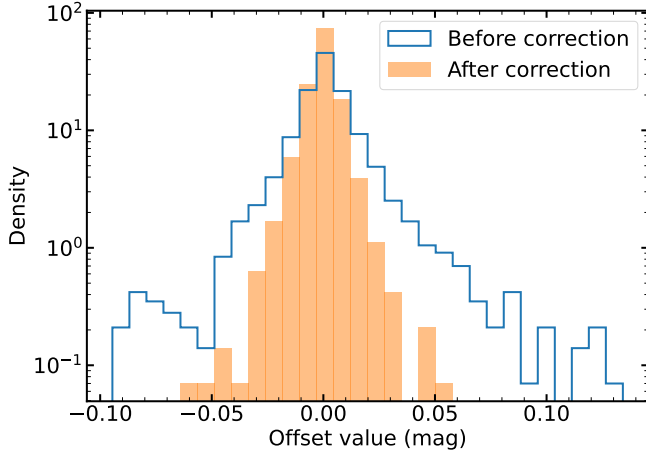


Figure 3. The density distribution of systematic photometric zero point offset of all the NIRCcam *visit* pairs that have more than 50 sources before (blue solid line histogram) and after correction (orange shaded histogram).

across all *visit* pairs gradually converging towards a self-consistent result. The final corrections are applied to the original data, significantly reducing the systematic photometric zero point offsets across all pairs. Figure 3 shows the density distribution of systematic photometric zero point offset of all the NIRCcam *visit* pairs before and after correction. Our correction greatly reduces the offsets, with the corrected offsets of most of the *visit* pairs being less than 0.02 mag. In this way, we do not accurately calibrate the absolute photometric zero point of each *visit*. However, we ensure that their relative photometric zero point is consistent, which is crucial in the variability analyses.

3.5. Calibration of Photometric Uncertainty

We calibrate the photometric uncertainties based on the variable source detection method described in previous works (e.g., Cohen et al. 2006; Kimura et al. 2020; O’Brien et al. 2024). This method assumes that most of the sources we observed are not variable. Thus, the scatter of the magnitude difference for a large sample of sources reflects the real photometric uncertainty. To minimize the uncertainty introduced by saturated pixels, truncated footprints, corrupted apertures/footprints, or other issues, we ignore objects with a SExtractor FLAGS > 1. We also ignore objects with SNR < 5 and contain bad pixels (IMAFLAGS_ISO ≠ 0). Lastly, as most of the LRDs are point-like sources, we restrict the sources to have ELONGATION < 1.5 to avoid the uncertainty introduced by the difference in morphology.

For each band in each common field, we plot the magnitude difference versus the mean magnitude combining all the *visit*-pair catalogs. As an example, Figure 4 dis-

plays the results for the F277W band in the GOODS-S field. We divide the data into magnitude bins with a bin size of ~ 0.5 mag and compute the 3σ clipped standard deviation of Δm ($\sigma_{\Delta m}$) and the median of Δm_{err} ($\langle \Delta m_{\text{err}} \rangle$) in each magnitude bin. The $\sigma_{\Delta m}$ and $\langle \Delta m_{\text{err}} \rangle$ are both fitted with a straight line in the bright end and with a third-order polynomial line in the faint end, with the two lines restricted to be smoothly connected. The error correction curve is derived as the difference between the $\sigma_{\Delta m}$ curve and the $\langle \Delta m_{\text{err}} \rangle$ curve.

When deriving the error correction curves, we also remove the LRDs and known AGNs in each field to avoid the influence of any variability of these sources. We collect AGN samples from the literature, and the details of the known AGN samples for each field are listed in Appendix (Table 5). For Abell 2744, there is no available AGN catalogs, and the fraction of typical AGNs should be relatively small in such a galaxy cluster field. Thus, we do not remove AGNs in this field.

Figure 5 shows the correction curves for different bands of the GOODS-S field as an example. The correction curves for LW and SW bands show different patterns. For the LW band, the correction increases with magnitude, while that decreases with magnitude and even becomes negative in the bright end for SW bands. We calibrate the error of Δm and m using the correction curves and the correction curves divided by the square root of two, respectively. We do the correction for each field separately, as we find that the correction curves also vary from field to field, likely caused by the different observational depths and dates. Lastly, we also set the minimum error for m and Δm to be 0.05 mag and 0.07 mag, respectively.

4. RESULTS

4.1. No Detection of Significant Variability for the Whole LRD Sample

Using the calibrated Δm and errors, we can measure the significance of the variability of an object between 2 *visits* as:

$$\text{SNR}_{\text{var}} = |\Delta m| / \Delta m_{\text{err}}, \quad (1)$$

where Δm and Δm_{err} are calibrated as described in Section 3.4 and Section 3.5, respectively. For a sample of non-variable sources, the distribution of their SNR_{var} should follow a standard Gaussian distribution. We plot the SNR_{var} distribution of all sources (with the criteria in Section 3.5) of each band and each field in Figure 6. One source can contribute multiple SNR_{var} values if it was observed in more than two *visits*. In Figure 6, we also plot the SNR_{var} distribution calculated using the uncalibrated Δm and errors and the standard

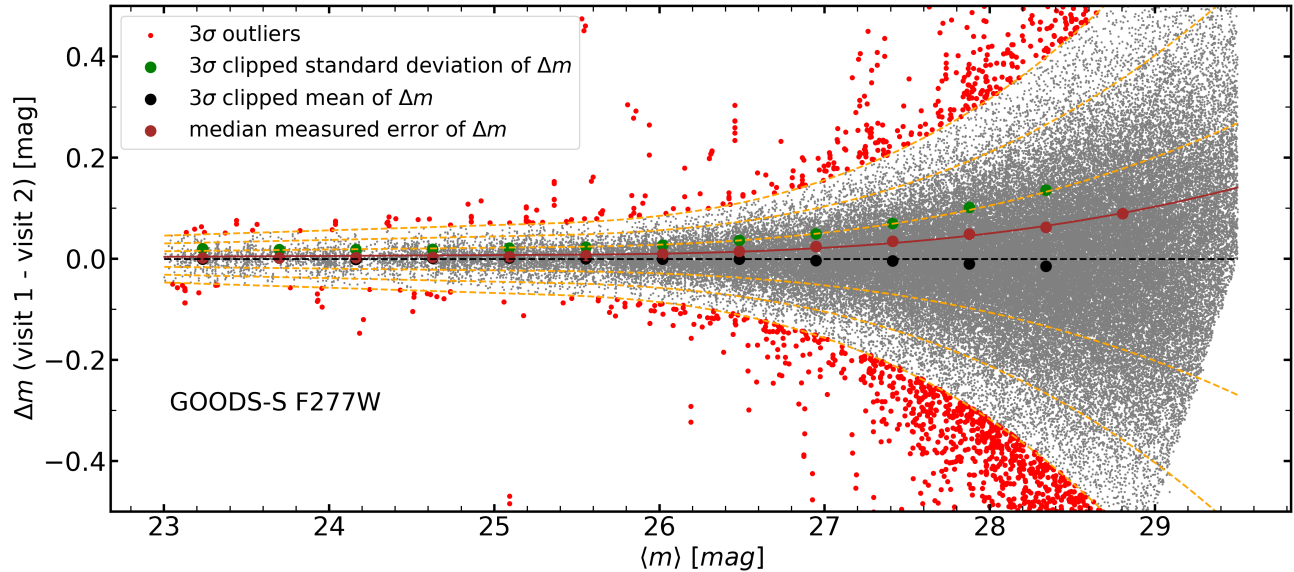


Figure 4. Magnitude difference versus the mean magnitude of the F277W band for the GOODS-S field. The small gray dots are the 3σ clipped sample used to calculate the mean and standard deviation of Δm in the magnitude bins, while the small red dots are clipped 3σ outliers. The green and black dots are the mean and standard deviation of Δm in each bin, respectively. The brown dots are the median values of the measured errors of Δm propagated from the errors of m_{visit1} and m_{visit2} . The yellow dashed curves are the 1σ , 2σ , and 3σ deviation from the mean value. The black dashed curves represent $\Delta m = 0$.

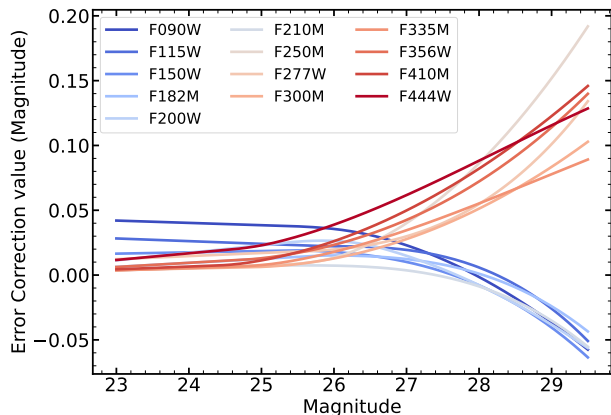


Figure 5. The Δm error correction curves of different bands for GOODS-S field.

Gaussian distribution for comparison. The SNR_{var} distributions calculated using the calibrated Δm and errors are consistent with the standard Gaussian distribution, confirming our error calibration’s reliability. The uncalibrated SNR_{var} distributions deviate from the standard Gaussian distribution, especially for the LW bands, which is consistent with the fact that we need to make a larger error correction to these bands (see Figure 5). As we set a minimum error of the measured magnitude as 0.05 mag, the calibrated SNR_{var} distributions are more concentrated towards 0 than the standard Gaussian distribution. The calibrated SNR_{var} distributions also have tails in their high SNR_{var} end. Visual checks of the

light curves and cut-out images of a random sample of the sources contributing to these tails find that some of them are real variable sources, while some of them are caused by image artifacts like cosmic rays, hot pixels, optical ghosts, etc.

We compare the SNR_{var} distribution of the LRD samples to that of fiducial samples to evaluate whether the LRD sample shows significant variability on average. The fiducial sample for each field is drawn from all the sources used in Section 3.5 with known AGNs and LRDs removed. We ensure that the fiducial sample has the same magnitude distribution as the LRD sample (all have large KS-test p value) and that the number of sources in the fiducial sample is 20 times the number of LRDs. Our data probe the variability of LRDs from $\sim 1500\text{\AA}$ to $\sim 8500\text{\AA}$, in the time scale of ~ 0.1 to ~ 100 days (see Figure 7). We tend to have more data points in the rest-frame optical than the rest-frame UV since LRDs are fainter in rest-frame UV and thus more difficult to have high SNR detection on a *visit* mosaic.

The results of the SNR_{var} distribution are shown in Figure 8. The LRD samples all show a nearly consistent SNR_{var} distribution with the fiducial samples except for the NIRCcam data of the UDS field. The high SNR_{var} in the UDS field is mainly caused by 3 LRDs, whose variability is found to be caused by the unique strip-like global background pollution in some *visits*. After removing these three problematic sources, the modified SNR_{var} distribution of LRDs (dashed blue step distribu-

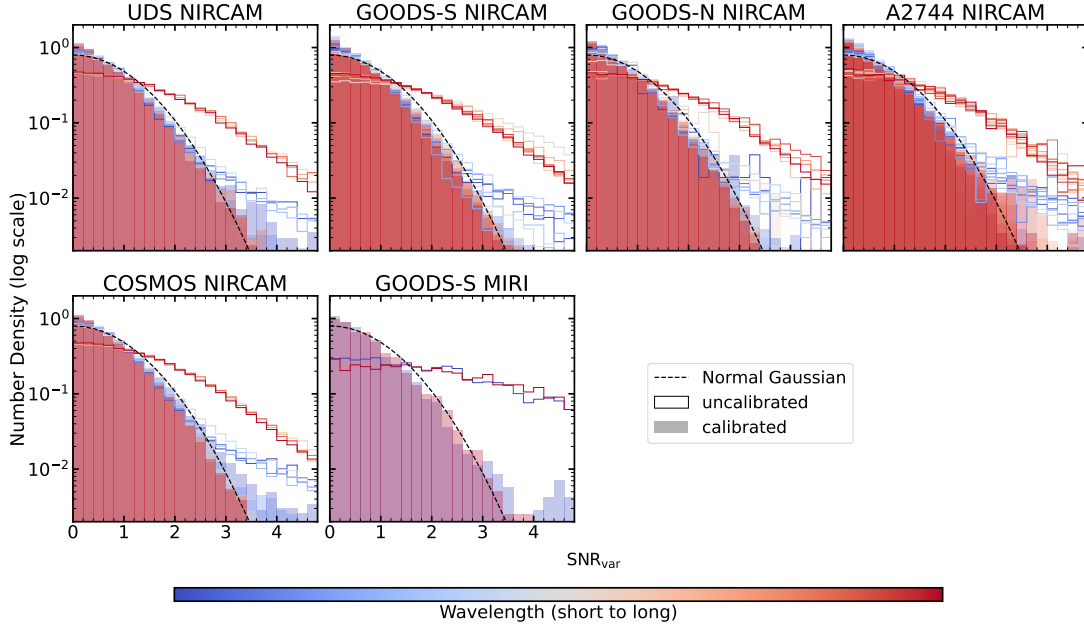


Figure 6. The distribution of SNR_{var} of all sources for each band for different fields. The shaded histograms represent the calibrated SNR_{var} distribution, with each band color-coded as indicated in the color bar at the bottom. The solid line histograms correspond to the SNR_{var} distribution calculated using the uncalibrated Δm and errors. The black dashed line shows the standard Gaussian distribution for comparison.

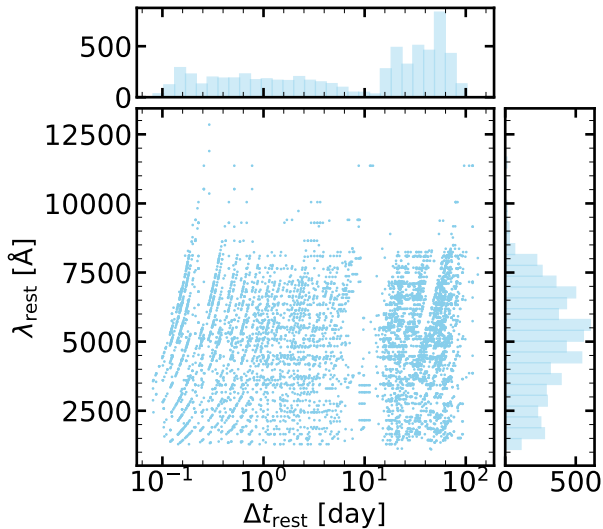


Figure 7. Data points of rest-frame time interval and rest-frame wavelength for the LRD sample. The histogram for each parameter is shown on each side.

tion in Figure 8(a)) is also consistent with the fiducial distribution for UDS field. For the NIRCAM data in the GOODS-N field and the MIRI data in the GOODS-S field, they only have 51 and 52 LRD pairs, respectively; thus, the expected number of pairs that show $\text{SNR}_{\text{var}} > 2$ (corresponding to $< 5\%$ for normalized Gaussian distribution) is smaller than one, which is consistent with our results. The SNR_{var} distribution com-

parison combining NIRCAM data from all fields in Figure 8(g), which has the highest statistical significance, also shows that the LRD distribution and fiducial distribution are almost the same. To conclude, these results indicate that at least most of the LRDs do not show detectable variability.

4.2. No Significant Variability of LRDs That Show Broad Emission Line

Among the 314 LRDs that have multi-epoch observation, 27 of them are revealed to show broad Balmer lines in the literature (Harikane et al. 2023; Akins et al. 2024a; Kocovski et al. 2024; Kokorev et al. 2024b; Greene et al. 2024; Maiolino et al. 2024; Matthee et al. 2024; Wang et al. 2024a; Williams et al. 2024). These sources are considered to be the most reliable AGN candidates within the LRD sample. We plot the SNR_{var} distribution of these broad-line LRDs in Figure 9. Their SNR_{var} distribution also shows no sign of variability compared with the fiducial distribution and the standard Gaussian distribution.

The broad $\text{H}\alpha$ emission of some LRDs are observed to have high equivalent widths (EWs; e.g., Maiolino et al. 2023; Wang et al. 2024a,b), which is similar to or generally higher than that expected for AGNs (e.g., the $L_{\text{H}\alpha} - L_{5100\text{\AA}}$ relation in Greene & Ho 2005). The continua of these LRDs should be dominated by AGNs at least at the bands that contain broad $\text{H}\alpha$ emission. Otherwise, the EWs would be lower. Therefore, we also plot the

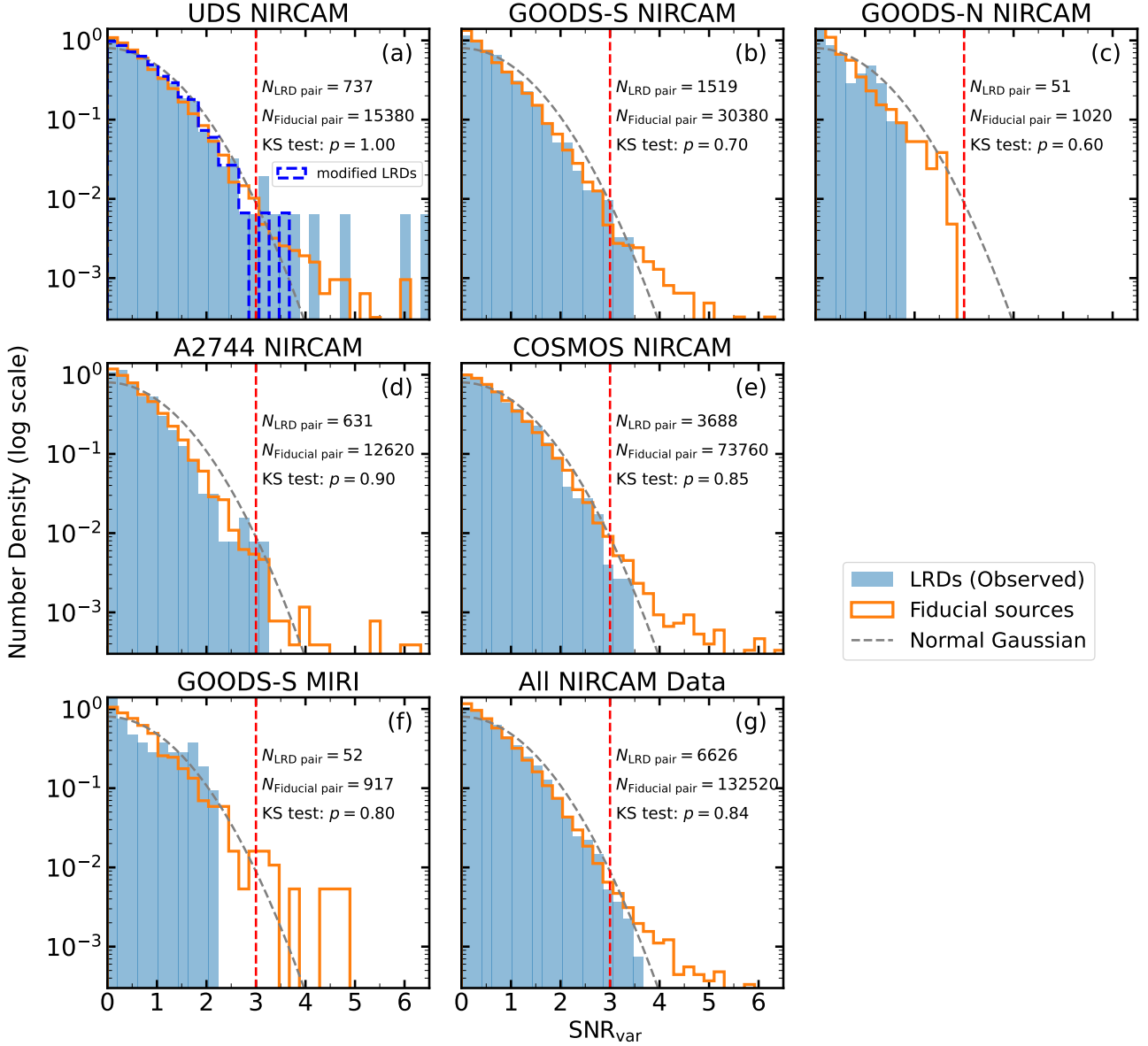


Figure 8. The SNR_{var} distribution of LRDs and the fiducial sources combining all bands. Panel (a)–(e) shows the distribution for NIRCcam data of UDS, GOODS-S, GOODS-N, Abell 2744, and COSMOS fields, respectively. Panel (f) shows the distribution of MIRI data of GOODS-S. Panel (g) shows the distribution for all NIRCcam data. The number of LRD pair, number of fiducial pair, and the KS-test p value are labeled in each panel. The standard Gaussian distribution is represented by a gray dashed line for comparison. The numbers of SNR_{var} values used to plot the distribution of the LRD sample and fiducial sample for each field are labeled in each panel. The red vertical dashed line is $\text{SNR}_{\text{var}} = 3$. SNR_{var} distribution of LRDs is almost the same as that of all other sources, indicating that most LRDs do not show significant variability.

SNR_{var} distribution of the filters that are expected to contain $\text{H}\alpha$ line based on their spec- z /photo- z for all LRDs in Figure 9. Nevertheless, this distribution also indicates no significant variability.

4.3. Eight Significantly Variable LRD Candidates

Although most of the LRDs do not show significant variability, there are still 10 LRDs that show variability of $\text{SNR}_{\text{var}} > 3$ in at least one *visit* pair. Visual inspec-

tion reveals that the variability of two of them is caused by the contamination of a nearby bright source and the cosmic ray, respectively. After removing these two sources, we identify eight variable LRD candidates. Table 4 summarizes the basic information of these sources. Their maximum variability amplitudes are 0.24 – 0.82 mag. A2744-14 (GLASS 150029 in Harikane et al. 2023) was also analyzed by Kokubo & Harikane (2024), but they reported no significant variability. We find that

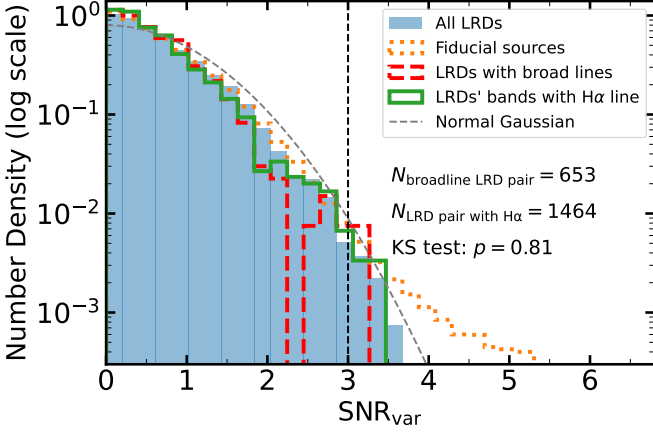


Figure 9. The SNR_{var} distribution of LRDs that show broad lines (red dashed line) and the filters with $\text{H}\alpha/\text{H}\beta$ line based on their spec- z /photo- z of all LRDs (green solid line). The full-LRD SNR_{var} distribution (blue) is the same as Figure 8(g). The fiducial SNR_{var} distribution is drawn to have same magnitude distribution as the broad-line LRD sample, with the KS-test p value of these two sample labeled.

A2744-14 shows variability of $\text{SNR}_{\text{var}} > 3$ in the F360M bands. This band is not included in Kokubo & Harikane (2024).

The color distribution of the eight variable LRD candidates is shown in Figure 1 to compare with the whole LRD sample. It seems that their colors tend to be relatively bluer. This indicates that the red color of those reddest LRDs may be caused by stellar emission, while LRDs that are relatively blue may have less host contamination and thus be able to exhibit the intrinsic variability of AGNs.

Considering that the SNR_{var} distribution of all LRDs in Figure 8(g) is in good agreement with the standard Gaussian distribution, it is likely that most of these variable LRD candidates are false detections. However, we suggest that at least two of them (COS-584 and COS-593) are reliable detections because of their relatively large variability amplitude and coordinated trend of variability in different bands. These two sources both come from the PRIMER-COSMOS field, in which, on average, there are relatively more observations per source (there are 3688/6631 LRD pairs for 114/314 LRDs in this field). In addition, in this field, different bands often have simultaneous observations, which is lacking in other fields. In the following, we provide detailed information about these two LRDs. Their multi-band light curves, multi-band and multi-epoch cut-out images, surface brightness (SB) profiles, and SEDs are shown in Figure 10 and Figure 12, respectively.

4.3.1. COS-584

COS-584 is selected by both Kocevski et al. (2024) and Kokorev et al. (2024a) as a LRD (their ID 25438 and ID 14086, respectively), with a photo- z of 7.127. It brightens for 0.82 mag in the F277W band between 2023-05-09 and 2023-12-28, which is the largest variability amplitude of the eight variable LRDs. Its light curves of the other band also show a coordinated trend with F277W but with smaller variability amplitude and SNR_{var} as shown in Figure 10(a). This multi-band coordination confirms the variability of COS-584. It shows a smaller variability amplitude in longer-wavelength bands, which is consistent with the expectation of AGNs.

The variability amplitude of 0.82 mag (corresponding to a factor of ≈ 2) constrains the AGN fraction in rest-frame $\sim 3500\text{\AA}$ to be $> 50\%$, which is helpful to break the degeneracy in SED fitting. We try to fit the JWST/NIRCam SED of COS-584 using CIGALE (Burgarella et al. 2005; Boquien et al. 2019) with this constraint (see Appendix for details), and the best-fit result is shown in Figure 11(a). The continuum of the best-fit model at and blueward F277W is dominated by the AGN component. The host contamination becomes large toward longer wavelengths and could dilute the intrinsic variability of the AGN, which can also partly explain the smaller variability amplitude in longer wavelength.

4.3.2. COS-593

COS-593 is also selected by both Kocevski et al. (2024) and Kokorev et al. (2024a) as a LRD (their ID 22990 and ID 17813, respectively). Its photo- z is 5.2 in both works. COS-593 shows a maximal variability of $\Delta m = 0.61$ in the F356W band with $\text{SNR}_{\text{var}} = 3.3$ between the observations on 2023-01-03 and 2023-12-09.

Although the maximal SNR_{var} values in the other three bands do not exceed 3, they all show a consistent variability trend. However, the variability trend of F356W is different from the other three bands. As shown in Figure 12(d), F277W, F410M, and F444W are all expected to enclose $\text{H}\alpha/\text{H}\beta$ line, while F356W is line-free, adopting a redshift of 5.2. The different trend of the light curves of F356W and the other bands may be caused by the lag between the emission line and continuum variability, which is expected for AGNs. The L_{5100} of the AGN from the best-fit SED model (see below) is $5 \times 10^{42} \text{ erg s}^{-1}$. Using the size-luminosity relation in Du et al. (2016), the lag of the $\text{H}\beta$ line is estimated to be ~ 10 days in the rest frame, corresponding to ~ 60 days in the observer frame. Assuming that the time scale of $\text{H}\alpha$ lag is similar to the $\text{H}\beta$ lag, the different trend of the light curves is likely to be caused by such lags since the sampling of the light curves is limited.

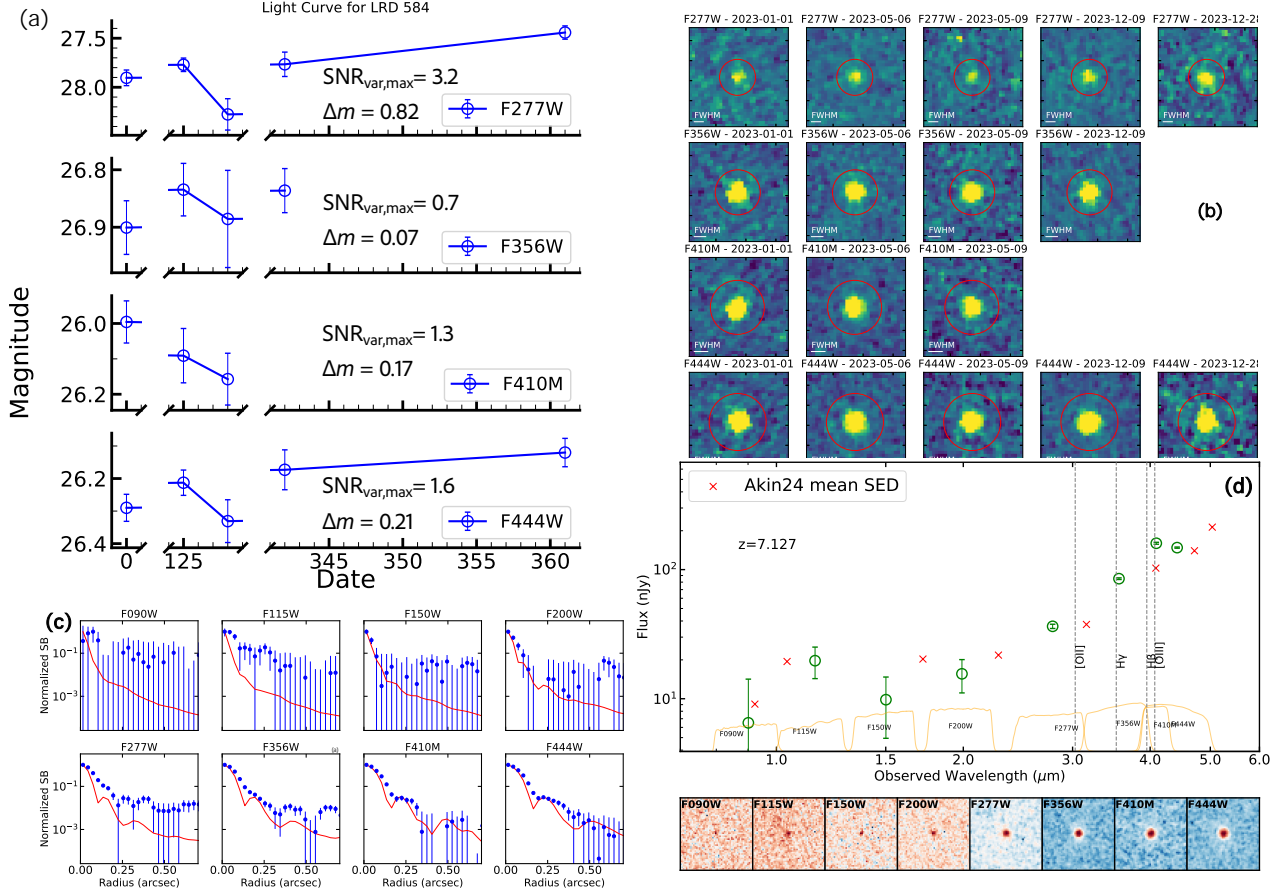


Figure 10. A kaleidoscope of COS-584. (a) The multi-band light curves, with the x-axis shows the observer-frame date, starting from the date of the first observation. The maximal $\text{SNR}_{\text{var,max}}$ and the corresponding Δm are noted for each band. (b) The multi-epoch cut-out images with size of $1''$. The band and observation date of each image are noted on the top. The red circles represent the photometric aperture with Section 3.3. Images of the same band use the same scale. (c) The SB profiles at different NIRCcam bands (blue errorbars). The SB profiles are normalised at the peak. The red curves show the SB profiles of JWST PSF obtain from *WebbPSF*. (d) The SED and mosaic cut-out images for different NIRCcam bands. The average SED of LRDs from *Akins et al. (2024a)* are shown for comparison. Main emission lines are indicated by vertical dotted lines.

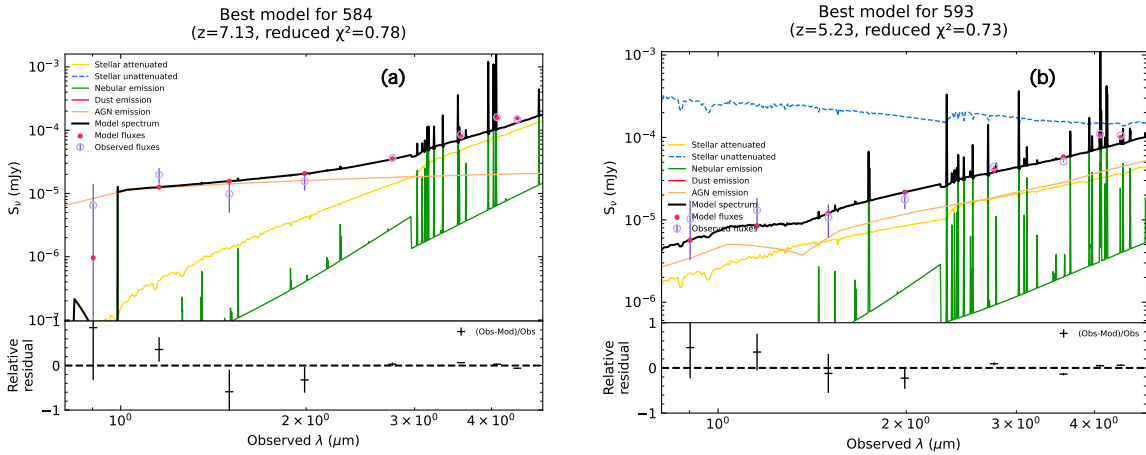


Figure 11. The best-fit SED models of (a) COS-584 and (b) COS-593 under the constraint of the AGN fraction set by their maximal variability amplitude as described in Section 4.3. The photometric points of the source and the inferred photometry, based on the components listed, are shown. The bottom panel displays the relative residuals between the observed and inferred photometry.

Table 4. LRDs that show variability of $\text{SNR}_{\text{var}} > 3$

LID	R.A.	Decl.	M_{UV}	z	ztype	isBL	$\log M_{\text{BH}}$	SF_{∞}	SNR_{var}	Δm	N_{band}	N_{obs}	band	date	ref
(1)	(2)	(3)	(4)	(5)	(6)	(7)	(8)	(9)	(10)	(11)	(12)	(13)	(14)	(15)	(16)
A2744-14	3.577167	-30.422583	-19.2	4.583	1	1	6.6	< -0.88	3.2	0.28	12	34	F360M	2023-10-31-2023-11-12	H23
UDS-108	34.363515	-5.176964	-19.2	4.317	0	0	...	< -1.24	3.6	0.25	6	19	F200W	2023-08-07-2023-08-09	K24a/K24b
UDS-147	34.411921	-5.144804	-18.2	7.630	0	0	...	< -0.26	3.2	0.71	2	4	F444W	2023-08-07-2023-08-09	K24a
GS-258	53.159333	-27.811749	-17.6	4.942	0	0	...	< -0.98	3.4	0.47	7	24	F410M	2022-10-03-2022-10-04	K24a/K24b
COS-538	150.111076	2.245270	-19.3	7.135	0	0	...	< -1.42	3.4	0.24	6	36	F410M	2023-04-27-2023-05-22	K24a/K24b/A24
COS-584	150.149360	2.252564	-17.7	7.127	0	0	...	< -0.14	3.2	0.82	4	17	F277W	2023-05-09-2023-12-28	K24a/K24b
COS-593	150.152769	2.273189	-17.5	5.227	0	0	...	< -0.02	3.3	0.61	4	21	F356W	2023-01-03-2023-12-09	K24a/K24b
COS-621	150.170181	2.388390	-20.1	5.367	0	0	...	< -1.68	3.1	0.47	8	35	F150W	2023-01-03-2023-12-29	K24a/K24b

NOTE—Col. (1): LID assigned in Section 2 according to the R.A. order. Cols. (2) and (3): Right Ascension and Declination. Col. (4): UV absolute magnitude adopted from Kocovski et al. (2024) and Harikane et al. (2023). Col. (5): Redshift adopted from Kocovski et al. (2024) and Harikane et al. (2023). Col. (6): Type of Redshift: 1 denotes spec- z and 0 denotes photo- z . Col. (7): Label indicates the presence of broad emission line: 1 means the LRD is revealed to have broad emission line and 0 means the LRD do not have spectroscopic observation yet. Col. (8): Black hole mass of A2744-14 adopted from Kocovski et al. (2024). Col. (9): Upper limit of $\text{SF}_{\infty}(4000\text{\AA})$ derived as described in Section 5.2. Col. (10): Maximal SNR_{var} value calculated as described in Section 4.1. Col. (11): The magnitude difference corresponds to the maximal SNR_{var} value. Col. (12): Total number of bands that have multi-epoch detections. Col. (13): Total number of multi-epoch detections with all bands combined. Col. (14): The band in which the maximal SNR_{var} value measured. Col. (15): The date pair on which the maximum SN value measured. Col. (16): The reference that select the object as a LRD or H α emitter. H23: Harikane et al. (2023); A24: Akins et al. (2024a); K24a: Kocovski et al. (2024); K24b: Kokorev et al. (2024a).

The SED of COS-584 is bluer than the average LRD SED from Akins et al. (2024a). The best-fit result of the JWST/NIRCam SED of COS-593 using CIGALE is shown in Figure 11(b), fitted with a constraint of AGN fraction $> 40\%$ at F356W band set by its variability amplitude. The best-fit result shows that the AGN and galaxy contribution is almost comparable across all wavelengths, which is consistent with the SB profile in Figure 12(c), showing that it has some degree of extended emission in all bands.

5. DISCUSSION

5.1. Effect of the Spatial Variation of PSF

Even for the NIRCam on JWST, it is not possible to achieve a perfect point spread function (PSF) that remains consistent over time and across different positions on the focal plane. Recent studies have demonstrated that the NIRCam PSF exhibits significant spatial variations of up to approximately 15–20% (e.g., Nardiello et al. 2022; Zhuang & Shen 2024), as well as temporal variations around 3–4% (e.g., Nardiello et al. 2022). The temporal variations are nearly negligible, and we have corrected the relative photometric zero point offset across different *visits* (see Section 3.4). The spatial variations are relatively large and may affect our results.

Here, we assess the extent to which PSF spatial variation affects our aperture photometry. Zhuang & Shen (2024) divided the field of NIRCam into 36 (6×6) regions and constructed reliable PSF models for each region using PSFEX. Using their spatial dependent PSF models for F070W, F115W, F150W, F200W, F277W, F356W, and F444W bands, we measure the curves of growth for the PSF models in different regions. We normalize the curves of growth at $1''$ for SW bands and at $1.2''$ for LW bands, where the curves of growth have flattened enough. Figure 13 shows the curves of growth divided by their mean curves for each band. It is obvious that at a small radius, the effect of PSF variation is significant, and it is mitigated going to a large radius. At the radius corresponding to our photometric aperture (2.5 pixels for F070W and $2 \times \text{FWHM}$ for other bands), the largest variation of the curves of growth caused by the PSF spatial variation is all $\sim 5\%$ (corresponds to 0.05 mag) for each band. Therefore, we can neglect the effects caused by the spatial variation of the PSF. We also try to use a larger radius (2.5 pixels for F070W and $2.5 \times \text{FWHM}$ for each band) and find that it does not significantly affect our result of the SNR_{var} distributions in Figure 6 and Figure 8. Therefore, we use $2 \times \text{FWHM}$ as the photometric radius, which mitigates the influence of PSF spatial variation and achieves relatively small measurement uncertainty.

5.2. Constraint on the Variability Amplitudes of LRDs

We do not observe significant variability, on average, in either the overall LRD sample or in the LRDs with broad emission lines (Section 4). The optical variability amplitude of AGN depends on the rest-frame wavelength, luminosity, Eddington ratio, BH mass, etc (e.g., Vanden Berk et al. 2004; MacLeod et al. 2011; Zuo et al. 2012). The host contamination also dilutes the variability of the central AGN. The LRDs and known AGNs in low redshift occupy different parameter spaces and it is hard to make direct comparison. In this section, we try to set constraints on the variability amplitudes of LRDs based on the damped random walk (DRW) model and compare them with the expectation of AGNs.

The AGN UV-optical continuum variability can be well described by the DRW model (Kelly et al. 2009; Kozłowski et al. 2010; MacLeod et al. 2010; Zu et al. 2011), which is shown to be able to recover the structure functions of AGNs (e.g., MacLeod et al. 2011). The structure function represents the root-mean-square (rms) of the magnitude differences Δm of a AGN sample in a given time interval Δt bin, i.e., typical variability amplitude at Δt . We set constraints on the asymptotic variability $\text{SF}_{\infty}(4000\text{\AA})$ of the LRDs adopting a DRW model likelihood (Kokubo & Harikane 2024, see Appendix for details).

Figure 14(a) displays $\text{SF}_{\infty}(4000\text{\AA})$ versus M_{BH} for the 27 LRDs with measured M_{BH} . Since we have calibrated the photometric errors and most of them become larger (see Section 3.5 and Figure 5), we get looser constraints for the same five sources compared with Kokubo & Harikane (2024). We also plot the empirical models from Burke et al. (2023) with varying host contamination factor f_* ,⁴ the observed values of $\text{SF}_{\infty}(4000\text{\AA})$ of the Sloan Digital Sky Survey (SDSS) Stripe82 quasars (MacLeod et al. 2010), and the Zwicky Transient Facility (ZTF) dwarf AGNs at $z \approx 0.03$ (Burke et al. 2023) for comparison. The Burke et al. (2023) model assumes an Eddington ratio of 0.1, $M_{\text{BH}}-M_*$ relation from Reines & Volonteri (2015), and stellar mass-to-light ratios of host galaxy color index of $g-r = 0.5$ mag.

For a significant number of LRDs in Figure 14, the upper limit constraints of the $\text{SF}_{\infty}(4000\text{\AA})$ indicate that

⁴ The observed host diluted rms variability amplitude is represented as: $\text{SF}'_{\infty} = \frac{L_{\text{AGN}}}{L_{\text{AGN}} + f_* L_*} \text{SF}_{\infty}$, where L_{AGN} , L_* and SF_{∞} are the mean AGN luminosity, the host galaxy luminosity in a given band, and the intrinsic rms variability amplitude of AGN, respectively. The contamination factor f_* (i.e., covering factor) accounts for the aperture effects, defined as the ratio between the host galaxy luminosity enclosed in an aperture and the total luminosity from the host galaxy starlight

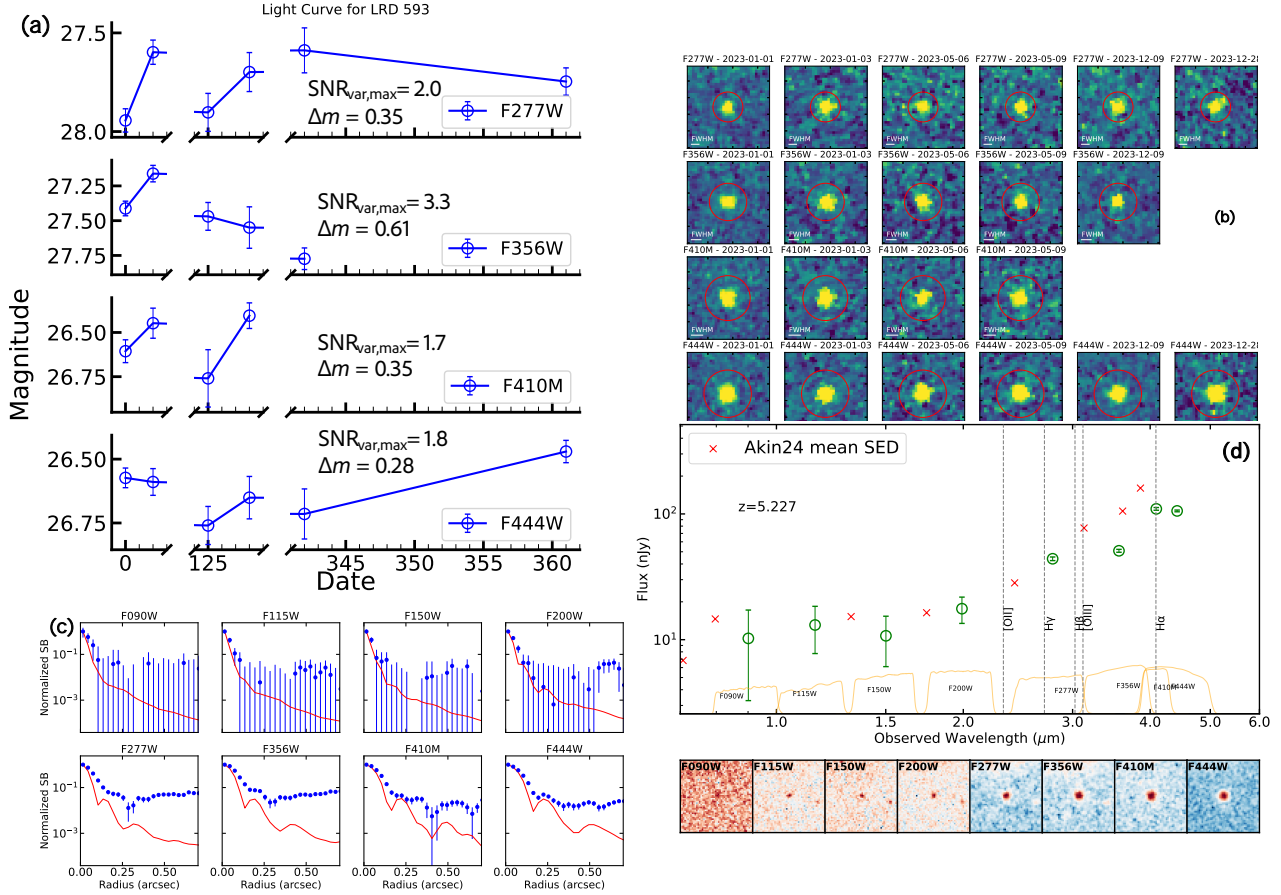


Figure 12. The same as Figure 10, but for COS-593.

their variability amplitudes are smaller than that expected for AGNs. The variability amplitudes for some LRDs are even smaller than the [Burke et al. \(2023\)](#) model with maximal host dilution ($f_* = 100\%$). However, assuming an Eddington ratio of 0.1 actually results in a model with the highest expected variability for dwarf AGNs. This is because higher Eddington ratios correspond to lower intrinsic variability, while lower Eddington ratios are associated with greater host contamination ([Burke et al. 2023](#)) and also have reduced variability amplitude. Since most LRDs are shown to host overmassive SMBHs compared to the local $M_{\text{BH}}-M_*$ relation (e.g., [Harikane et al. 2023](#); [Larson et al. 2023](#); [Maiolino et al. 2023](#)), their host contamination should be smaller than typical AGNs or local dwarf AGNs. Therefore, the non-detection of variability of these sources indicates that they may be intrinsically not variable.

There are also some LRDs have $\text{SF}_\infty(4000\text{\AA})$ upper limits > -1 . This does not necessarily mean they are variable, as the upper limit here is a conservative value because of our assumption above and the limited sampling. The histogram of the $\text{SF}_\infty(4000\text{\AA})$ upper limits for all 314 LRDs in Figure 14(b) shows that sources with more multi-epoch observations (e.g., > 20 obser-

vations in all bands) tend to have lower $\text{SF}_\infty(4000\text{\AA})$ upper limit constraints. We also check the 11 LRDs that have $\sigma_d(4000\text{\AA})$ upper limits > -1 in Figure 14(a) and find that 10 of them do not show SNR_{var} value of larger than 2. Therefore, most of these sources are not variable either.

5.3. High Accretion Rate Induced Lack of Variability?

In this section, we further suggest that the absence of variability may be due to the high accretion rates of the BHs in LRDs. Previous works found that the variability amplitude of AGNs decreases with the increase of Eddington ratio in a given bolometric luminosity (L_{bol} ; e.g., [MacLeod et al. 2010](#); [Zuo et al. 2012](#)). In the low redshift, AGNs with very high accretion rates, such as narrow-line Seyfert 1 (NLS1) galaxies, are found to show very low level of optical variability (e.g., [Klimek et al. 2004](#); [Du et al. 2016](#)). Given that the estimated Eddington ratios of LRDs fall in the super-Eddington or sub-Eddington regimes (e.g., [Harikane et al. 2023](#); [Maiolino et al. 2023](#)), it is possible that their lack of variability could be linked to the high accretion rates. Here, we simulate the expected SNR_{var} distribution of LRDs to test this hypothesis.

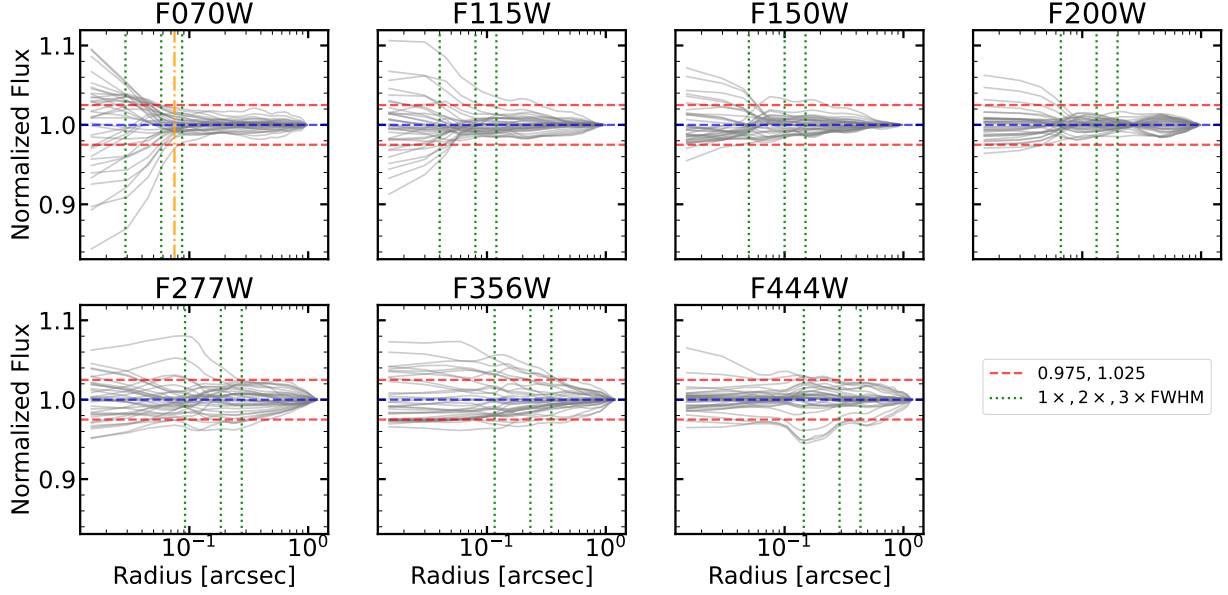


Figure 13. Normalized curves of growth of spatial dependent PSF models from Zhuang & Shen (2024) for different bands. The gray lines are the curves of growth of PSF models in different regions normalized by their mean curve of growth. The PSF models are normalized at $1''$ for SW bands and $1''.2$ for LW bands. The vertical green dotted lines show the radius corresponding to $1\times$, $2\times$, and $3\times$ FWHM. The vertical yellow dashdot line for the F070W band is the radius corresponding to 2.5 pixels used for photometry. The horizontal red dashed lines correspond to 0.975 and 1.025.

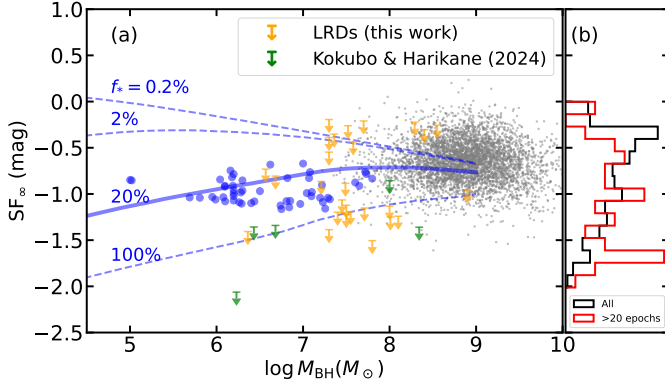


Figure 14. (a) The asymptotic variability $SF_{\infty}(4000\text{\AA})$ versus M_{BH} . The yellow downward arrows represent the upper limit of $SF_{\infty}(4000\text{\AA})$ at 90% confidence level for the 27 LRDs with M_{BH} measurements. The SMBH masses are collected from the literature (Section 2). The green downward arrows are the 5 LRDs in Kokubo & Harikane (2024). The blue and black points are the ZTF dwarf AGNs from Burke et al. (2023) and the SDSS Stripe82 quasars from MacLeod et al. (2010), respectively. The thick solid and thin dashed lines indicate the Burke et al. (2023)’s empirical model of SF_{∞} with varying host dilution covering factors around 0.2%–100%. (b) The distribution of $SF_{\infty}(4000\text{\AA})$ for all 314 LRDs that have multi-epoch observation (black line) and for LRDs that have more than 20 observation across all bands (red line).

We adopt the structure function model from Kimura et al. (2020), which considers the dependence on rest-frame wavelength λ_{rest} , L_{bol} , and rest-frame time in-

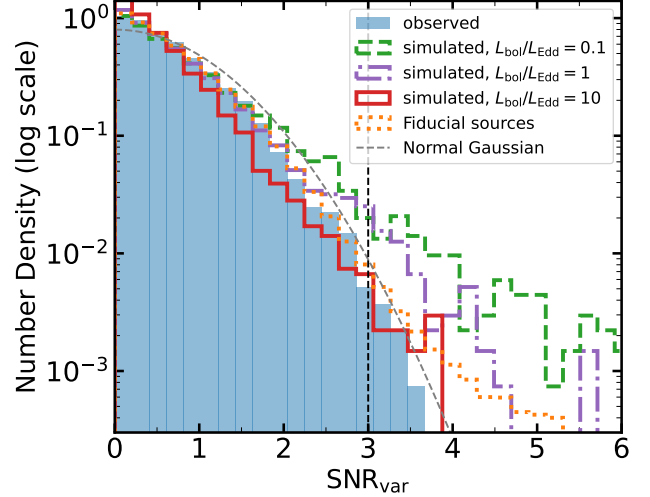


Figure 15. The observed and simulated SNR_{var} distribution of the LRD sample for all NIRCcam data. The observed LRD distribution and fiducial source distribution are the same as Figure 8(g). The green dashed line, purple dot-dash line, and red solid line correspond to the simulated LRD distribution with $L_{\text{bol}}/L_{\text{Edd}} = 0.1, 1, 10$, respectively

terval Δt_{rest} (see their Equations 13–22 and Table 7). These three parameters are already determined from observations, and an expected SF value can be derived for each pair. However, their structure function does not consider the dependence on the Eddington ratio, which

we introduce using Equation 9 from [Burke et al. \(2023\)](#):

$$\log\left(\frac{\text{SF}_\infty}{\text{mag}}\right) = -0.51 - 0.479 \log\left(\frac{\lambda_{\text{rest}}}{4000 \text{ \AA}}\right) + 0.131(M_i + 23) + 0.18 \log\left(\frac{M_{\text{BH}}}{10^9 M_\odot}\right). \quad (2)$$

We substitute $\frac{M_{\text{BH}}}{M_\odot} = L_{\text{bol}}/\lambda_{\text{Edd}}/(1.28 \times 10^{38} \text{ erg s}^{-1})$. First, we solve Equation 2 to derive the effective Eddington ratio for each pair by using the $\text{SF}_\infty(4000\text{\AA})$ value provided by the structure function model in [Kimura et al. \(2020\)](#) and τ_d value (see Appendix) calculated using the Equation 10 in [Burke et al. \(2023\)](#). We then apply Equation 2 to scale the SF value to the target Eddington ratio. Here we assume that the λ_{Edd} dependence in Equation 2 can be extrapolated to high λ_{Edd} regime. For each pair, the expected observed Δm value is the intrinsic variability randomly drawn from a Gaussian distribution $\mathcal{N}(0, \text{SF}^2)$ plus a measurement uncertainty randomly drawn from $\mathcal{N}(0, \Delta m_{\text{err}}^2)$. The simulated SNR_{var} value is the ratio of the expected Δm and the real measured error Δm_{err} .

We compare the simulated and observed SNR_{var} distribution of LRDs in Figure 15. For simplicity, our simulated distributions assume that all LRDs have the same Eddington ratio of 0.1, 1, and 10, respectively. In the relatively low Eddington ratio case ($\lambda_{\text{Edd}} = 0.1$), we expect a broader SNR_{var} distribution than the observed one. However, the simulated distribution matches the observed distribution well when assuming super-Eddington accretions ($\lambda_{\text{Edd}} = 10$).

Both analytical studies and radiation hydrodynamic (RHD) simulations suggest that BHs with very high accretion rates do not necessarily produce proportionally high radiative luminosities (e.g., [Watarai et al. 2000](#); [Sadowski 2009](#); [Jiang et al. 2014](#)). BHs with accretion rates of $\dot{M}/M_{\text{Edd}} = 10^1\text{--}10^3$ exhibit radiative luminosities only within the range of 1–10 L_{Edd} (e.g., Figure 5 of [Inayoshi et al. 2020](#)). While some LRDs display measured Eddington ratios below or near the super-Eddington threshold, they may have very high intrinsic accretion rates, potentially explaining their low variability amplitudes. This super-Eddington accretion scenario could also naturally account for the X-ray weakness of LRDs (e.g., [Madau & Haardt 2024](#); [Pacucci & Narayan 2024](#)). Alternatively, these two features could be consistent with LRDs being galaxy-dominated systems. However, the high EWs of broad H α emission and the presence of O I lines observed in certain LRDs are more in line with the expected signatures of super-Eddington accreting BHs ([Inayoshi et al. 2022](#); [Inayoshi & Maiolino 2024](#)).

6. CONCLUSION

In this study, we conduct a comprehensive investigation of the photometric variability of LRDs based on all publicly available multi-wavelength multi-epoch NIR-Cam data in five JWST deep fields: UDS, GOODS-S, GOODS-N, Abell 2744, and COSMOS. We also incorporate available multi-epoch JWST/MIRI data in the GOODS-S field. We compile a large sample of 806 LRDs in these five fields from the literature and find 314 of them have multi-epoch detections. With correction of systematic photometric zero point offsets and calibration of photometric uncertainties, we evaluate the variability of these LRDs using the distribution of the signal-to-noise ratio of their variability (SNR_{var}).

The SNR_{var} distribution of LRDs is consistent with the fiducial distribution and the standard Gaussian distribution across five fields, which indicates that these 314 LRDs on average do not show significant photometric variability. This result persists even for the 27 LRDs that exhibit broad H α /H β lines, which are considered to be the most reliable candidates of AGNs within the LRD sample. The estimated conservative upper limits on the DRW asymptotic variability amplitude for quite a few LRDs are inconsistent with that observed in known AGNs, even if significant host galaxy contamination is considered. These results indicate that LRDs show very low variability amplitude intrinsically, which might be caused by the super-Eddington accretion of the BHs, or they are actually dominated by pure galaxies. We test the former scenario and find that the observed SNR_{var} distribution of LRDs can be well simulated under the assumption that LRDs have very high accretion rates.

Despite the overall lack of variability, we also find eight LRDs that show variability of $\text{SNR}_{\text{var}} > 3$, with variability amplitudes ranging from 0.24 to 0.82 mag. These objects stand out as reliable candidates that show AGN activity, though some of them could be false detection. We suggest that the variability of two of them (COS-584 and COS-593) are reliable detections because of their relatively large variability amplitude and coordinated trend of variability in different bands.

Our results demonstrate that the multi-epoch observations of JWST can be used to study the variability of a large sample of LRDs and offer new insights into their nature. However, the poor temporal sampling and short time baseline for many LRDs in our sample can still be improved in future studies. The upcoming COSMOS-3D Survey ([Kakiichi et al. 2024](#)) will perform new observations of F115W band in the COSMOS field, which combined with the F115W imaging from the COSMOS-Web Survey ([Casey et al. 2023](#)) can provide multi-epoch observations for most of the LRDs in this field with long

temporal coverage. Combing the multi-epoch JWST imaging/spectroscopic data from the upcoming North ecliptic pole EXtragalactic Unified Survey (NEXUS; Shen et al. 2024) and the existing JWST North Ecliptic Pole Time-Domain Field (NEP-TDF; Jansen & Windhorst 2018; O’Brien et al. 2024) can also provide multi-epoch observations with high sampling and long temporal coverage for LRDs in this field. Moreover, the rich multi-epoch data from JWST can independently identify high-redshift faint AGNs that are missed by other methods through variability, as demonstrated by Hayes et al. (2024) using multi-epoch HST data.

1 We acknowledge support from the National Key
 2 R&D Program of China (2022YFF0503401), the Na-
 3 tional Science Foundation of China (12225301,11991052,
 4 12233001), and the China Manned Space Project (CMS-
 5 CSST-2021-A04, CMS-CSST-2021-A05, CMS-CSST-
 6 2021-A06). We thank Kohei Inayoshi, Danyang Jiang,
 7 Fengwu Sun, Wei Leong Tee, and Feige Wang for help-
 8 ful discussions. We thank Mingyang Zhuang for sharing
 9 the spatial dependent PSF models of NIRCcam in their
 10 paper.

Facilities: JWST (NIRCcam, MIRI)

Software: `astropy` (Astropy Collaboration et al. 2013, 2018), `CIGALE` (Burgarella et al. 2005; Boquien et al. 2019), `dynesty` (Speagle 2020; Koposov et al. 2024), `matplotlib` (Hunter 2007), `numpy` (Harris et al. 2020), `SExtractor` (Bertin & Arnouts 1996), `TOPCAT` (Taylor 2005), `WebbPSF` (Perrin et al. 2014)

APPENDIX

A. ESTIMATION OF THE UPPER LIMIT OF THE ASYMPTOTIC VARIABILITY $SF_{\infty}(4000\text{\AA})$

The DRW model characterizes quasar light curves as stochastic process with an exponential covariance function $S(\Delta t) = \sigma_d^2 \exp(-|\Delta t/\tau_d|)$, where σ_d is an amplitude parameter and τ_d is the decorrelation time scale. The amplitude parameter is related to the structure function as: $SF_{\infty}(\lambda) = \sqrt{2}\sigma_d(\lambda)$, where $SF_{\infty} = SF(\Delta t > \tau_d)$ is the asymptotic variability amplitude that represents the asymptotic value of structure function when the time lag between observations Δt exceeds the timescale τ_d (MacLeod et al. 2010). The variability amplitude is usually modeled by a wavelength-dependent power-law (e.g., MacLeod et al. 2010; Kimura et al. 2020):

$$\sigma_d(\lambda) = \sigma_d(4000\text{\AA}) \left(\frac{\lambda}{4000\text{\AA}} \right)^{\alpha_{\text{var}}}. \quad (\text{A1})$$

We adopt the light curve data likelihood of the DRW model described in the Section 3.2 and Appendix of Kokubo & Harikane (2024), which is expressed by a multivariate Gaussian, to set constraints on the variability amplitude of LRDs. The current time sampling of the data is limited (see Figure 7), so the decorrelation time scale can not be well constrained. We use the empirical relation from Burke et al. (2023) to set a fixed value of τ_d for each LRD as done by Kokubo & Harikane (2024). For those LRDs without BH mass measurement, we assume $\tau_d = 70$ days, which is calculated using the median BH mass of LRDs. We find that in most cases, the degeneracy between $\sigma_d(4000\text{\AA})$ and τ_d is weak. Thus, the effect of this assumption is small. We also assume that the variability amplitude is independent of rest-wavelength. In this way, we can get a conservative upper limit on $\sigma_d(4000\text{\AA})$. Therefore, the final likelihood has only one free parameter: $\sigma_d(4000\text{\AA})$. We estimate its posterior for each source using the *dynesty* package (Speagle 2020; Koposov et al. 2024), which is based on the advanced Dynamic Nested Sampling algorithm (Higson et al. 2019). The prior of $\log \sigma_d(4000\text{\AA})$ is set as a uniform distribution between -4 and 0 . We calculate the 90% confidence level upper limit of $\log \sigma_d(4000\text{\AA})$ from the estimated posterior distribution of each source.

B. SAMPLES OF KNOWN AGNS IN EACH FIELD

Table 5 summarizes the known AGN samples used in this work.

C. SED FITTING SETUP

Table 6 summarizes the adopted parameters of `CIGALE`. We consider both a stellar component and an AGN component. The constraint of AGN fraction is set by adjusting the allowed values of frac_{AGN} and λ_{AGN} .

Table 5. Samples of known AGNs that are removed in Section 3.5.

Fields	Known AGN Sample
UDS	X-ray sources classified as AGNs in Chen et al. (2018) X-ray sources classified as AGNs in Kocevski et al. (2018)
GOODS-S	all sources in Lyu et al. (2022) and Lyu et al. (2024) that meet the AGN criteria in at least one band or via variability
GOODS-N	X-ray sources classified as AGN in Xue et al. (2016) VLBI detected radio AGNs in Radcliffe et al. (2018)
COSMOS	X-ray sources spectroscopically identified as AGNs or with $L_{2-10\text{keV}} > 10^{42} \text{ erg s}^{-1}$ in Brusa et al. (2010) X-ray sources spectroscopically identified as AGNs or with $L_{2-10\text{keV}} > 10^{42} \text{ erg s}^{-1}$ in Marchesi et al. (2016) 692 AGN-host systems detected both in the X-ray and FIR from Lanzuisi et al. (2017) AGNs selected by optically variability in De Cicco et al. (2019)

Table 6. CIGALE model parameters

Module	Parameter	Symbol	Values
Star formation history <code>sfhdelayed</code>	Stellar e-folding time	τ_{star}	0.2, 0.5, 1, 2, 3, 4, 5 Gyr
	Stellar age	t_{star}	0.1, 0.2, 0.5, 1, 2, 3, 4, 5, 7 Gyr
Simple stellar population <code>bc03</code>	Initial mass function	—	?
	Metallicity	Z	0.02
Nebular emission <code>nebular</code>	Ionization parameter	$\log U$	-4.0, -2.0
	Gas metallicity	Z_{gas}	0.0004, 0.002, 0.033
	Fraction of escaped Lyman continuum photons	f_{esc}	0.0, 0.05, 0.1, 0.5, 0.7, 1.0
Dust attenuation <code>dustatt_modified_starburst</code>	Color excess of nebular lines	$E(B - V)_{\text{line}}$	0,0.02,0.05,0.1,0.2, 0.3,0.4,0.5,0.7,0.9,1.0
	ratio between line and continuum $E(B - V)$	$\frac{E(B-V)_{\text{line}}}{E(B-V)_{\text{cont}}}$	0.44, 0.8, 1
Galactic dust emission <code>dl2014</code>	PAH mass fraction	q_{PAH}	0.47, 2.5, 7.32
	Minimum radiation field	U_{min}	0.1, 1.0, 10, 50
	Fraction of PDR emission	γ	0.01, 0.02, 0.05, 0.1, 0.2, 0.5, 0.9
AGN (UV-to-IR) emission <code>skirtor2016</code>	Average edge-on optical depth at $9.7\mu\text{m}$	$\tau_{9.7}$	3.5,7,9,11
	Viewing angle	θ_{AGN}	$30^\circ, 70^\circ$
	AGN contribution at given wavelength	frac_{AGN}	$(0.4^1), 0.5, 0.6, 0.7, 0.8, 0.9, 0.95, 0.99$
	Wavelength range where frac_{AGN} is defined	λ_{AGN}	0.3450/0.3470 μm (COS-584) 0.5730/0.5750 μm (COS-593)
Redshift+IGM <code>redshifting</code>	Source redshift	z	fixed as phot-zs

NOTE. — For parameters not listed here, default values are being adopted. ¹ for COS-593.

REFERENCES

- Aihara, H., AlSayyad, Y., Ando, M., et al. 2022, PASJ, 74, 247, doi: [10.1093/pasj/psab122](https://doi.org/10.1093/pasj/psab122)
- Akins, H. B., Casey, C. M., Allen, N., et al. 2023, ApJ, 956, 61, doi: [10.3847/1538-4357/acef21](https://doi.org/10.3847/1538-4357/acef21)
- Akins, H. B., Casey, C. M., Lambrides, E., et al. 2024a, arXiv e-prints, arXiv:2406.10341, doi: [10.48550/arXiv.2406.10341](https://doi.org/10.48550/arXiv.2406.10341)

- Akins, H. B., Casey, C. M., Berg, D. A., et al. 2024b, arXiv e-prints, arXiv:2410.00949, doi: [10.48550/arXiv.2410.00949](https://doi.org/10.48550/arXiv.2410.00949)
- Alberts, S., Lyu, J., Shivaee, I., et al. 2024, arXiv e-prints, arXiv:2405.15972, doi: [10.48550/arXiv.2405.15972](https://doi.org/10.48550/arXiv.2405.15972)
- Álvarez-Márquez, J., Crespo Gómez, A., Colina, L., et al. 2023, *A&A*, 671, A105, doi: [10.1051/0004-6361/202245400](https://doi.org/10.1051/0004-6361/202245400)
- Ananna, T. T., Bogdán, Á., Kovács, O. E., Natarajan, P., & Hickox, R. C. 2024, *ApJL*, 969, L18, doi: [10.3847/2041-8213/ad5669](https://doi.org/10.3847/2041-8213/ad5669)
- Astropy Collaboration, Robitaille, T. P., Tollerud, E. J., et al. 2013, *A&A*, 558, A33, doi: [10.1051/0004-6361/201322068](https://doi.org/10.1051/0004-6361/201322068)
- Astropy Collaboration, Price-Whelan, A. M., Sipőcz, B. M., et al. 2018, *AJ*, 156, 123, doi: [10.3847/1538-3881/aabc4f](https://doi.org/10.3847/1538-3881/aabc4f)
- Baggen, J. F. W., van Dokkum, P., Labbé, I., et al. 2023, *ApJL*, 955, L12, doi: [10.3847/2041-8213/acf5ef](https://doi.org/10.3847/2041-8213/acf5ef)
- Baggen, J. F. W., van Dokkum, P., Brammer, G., et al. 2024, arXiv e-prints, arXiv:2408.07745, doi: [10.48550/arXiv.2408.07745](https://doi.org/10.48550/arXiv.2408.07745)
- Bagley, M. B., Finkelstein, S. L., Koekemoer, A. M., et al. 2023, *ApJL*, 946, L12, doi: [10.3847/2041-8213/acbb08](https://doi.org/10.3847/2041-8213/acbb08)
- Barro, G., Pérez-González, P. G., Kocevski, D. D., et al. 2024, *ApJ*, 963, 128, doi: [10.3847/1538-4357/ad167e](https://doi.org/10.3847/1538-4357/ad167e)
- Bertin, E., & Arnouts, S. 1996, *A&AS*, 117, 393, doi: [10.1051/aas:1996164](https://doi.org/10.1051/aas:1996164)
- Bezanson, R., Labbe, I., Whitaker, K. E., et al. 2022, arXiv e-prints, arXiv:2212.04026, doi: [10.48550/arXiv.2212.04026](https://doi.org/10.48550/arXiv.2212.04026)
- Boquien, M., Burgarella, D., Roehlly, Y., et al. 2019, *A&A*, 622, A103, doi: [10.1051/0004-6361/201834156](https://doi.org/10.1051/0004-6361/201834156)
- Brusa, M., Civano, F., Comastri, A., et al. 2010, *ApJ*, 716, 348, doi: [10.1088/0004-637X/716/1/348](https://doi.org/10.1088/0004-637X/716/1/348)
- Burgarella, D., Buat, V., & Iglesias-Páramo, J. 2005, *MNRAS*, 360, 1413, doi: [10.1111/j.1365-2966.2005.09131.x](https://doi.org/10.1111/j.1365-2966.2005.09131.x)
- Burke, C. J., Shen, Y., Liu, X., et al. 2023, *MNRAS*, 518, 1880, doi: [10.1093/mnras/stac2478](https://doi.org/10.1093/mnras/stac2478)
- Casey, C. M., Kartaltepe, J. S., Drakos, N. E., et al. 2023, *ApJ*, 954, 31, doi: [10.3847/1538-4357/acc2bc](https://doi.org/10.3847/1538-4357/acc2bc)
- Chen, C. T. J., Brandt, W. N., Luo, B., et al. 2018, *MNRAS*, 478, 2132, doi: [10.1093/mnras/sty1036](https://doi.org/10.1093/mnras/sty1036)
- Cohen, S. H., Ryan, R. E., J., Straughn, A. N., et al. 2006, *ApJ*, 639, 731, doi: [10.1086/499577](https://doi.org/10.1086/499577)
- De Cicco, D., Paolillo, M., Falocco, S., et al. 2019, *A&A*, 627, A33, doi: [10.1051/0004-6361/201935659](https://doi.org/10.1051/0004-6361/201935659)
- DeCoursey, C., Egami, E., Pierel, J. D. R., et al. 2024, arXiv e-prints, arXiv:2406.05060, doi: [10.48550/arXiv.2406.05060](https://doi.org/10.48550/arXiv.2406.05060)
- Du, P., Lu, K.-X., Zhang, Z.-X., et al. 2016, *ApJ*, 825, 126, doi: [10.3847/0004-637X/825/2/126](https://doi.org/10.3847/0004-637X/825/2/126)
- Eisenstein, D. J., Willott, C., Alberts, S., et al. 2023a, arXiv e-prints, arXiv:2306.02465, doi: [10.48550/arXiv.2306.02465](https://doi.org/10.48550/arXiv.2306.02465)
- Eisenstein, D. J., Johnson, B. D., Robertson, B., et al. 2023b, arXiv e-prints, arXiv:2310.12340, doi: [10.48550/arXiv.2310.12340](https://doi.org/10.48550/arXiv.2310.12340)
- Furtak, L. J., Zitrin, A., Plat, A., et al. 2023, *ApJ*, 952, 142, doi: [10.3847/1538-4357/acdc9d](https://doi.org/10.3847/1538-4357/acdc9d)
- Greene, J. E., & Ho, L. C. 2005, *ApJ*, 630, 122, doi: [10.1086/431897](https://doi.org/10.1086/431897)
- Greene, J. E., Labbe, I., Goulding, A. D., et al. 2024, *ApJ*, 964, 39, doi: [10.3847/1538-4357/ad1e5f](https://doi.org/10.3847/1538-4357/ad1e5f)
- Guia, C. A., Pacucci, F., & Kocevski, D. D. 2024, *Research Notes of the American Astronomical Society*, 8, 207, doi: [10.3847/2515-5172/ad7262](https://doi.org/10.3847/2515-5172/ad7262)
- Harikane, Y., Zhang, Y., Nakajima, K., et al. 2023, *ApJ*, 959, 39, doi: [10.3847/1538-4357/ad029e](https://doi.org/10.3847/1538-4357/ad029e)
- Harris, C. R., Millman, K. J., van der Walt, S. J., et al. 2020, *Nature*, 585, 357, doi: [10.1038/s41586-020-2649-2](https://doi.org/10.1038/s41586-020-2649-2)
- Hayes, M. J., Tan, J. C., Ellis, R. S., et al. 2024, *ApJL*, 971, L16, doi: [10.3847/2041-8213/ad63a7](https://doi.org/10.3847/2041-8213/ad63a7)
- Higson, E., Handley, W., Hobson, M., & Lasenby, A. 2019, *Statistics and Computing*, 29, 891, doi: [10.1007/s11222-018-9844-0](https://doi.org/10.1007/s11222-018-9844-0)
- Hunter, J. D. 2007, *Computing in Science & Engineering*, 9, 90, doi: [10.1109/MCSE.2007.55](https://doi.org/10.1109/MCSE.2007.55)
- Iani, E., Rinaldi, P., Caputi, K. I., et al. 2024, arXiv e-prints, arXiv:2406.18207, doi: [10.48550/arXiv.2406.18207](https://doi.org/10.48550/arXiv.2406.18207)
- Inayoshi, K., & Maiolino, R. 2024, arXiv e-prints, arXiv:2409.07805, doi: [10.48550/arXiv.2409.07805](https://doi.org/10.48550/arXiv.2409.07805)
- Inayoshi, K., Onoue, M., Sugahara, Y., Inoue, A. K., & Ho, L. C. 2022, *ApJL*, 931, L25, doi: [10.3847/2041-8213/ac6f01](https://doi.org/10.3847/2041-8213/ac6f01)
- Inayoshi, K., Visbal, E., & Haiman, Z. 2020, *ARA&A*, 58, 27, doi: [10.1146/annurev-astro-120419-014455](https://doi.org/10.1146/annurev-astro-120419-014455)
- Jansen, R. A., & Windhorst, R. A. 2018, *PASP*, 130, 124001, doi: [10.1088/1538-3873/aae476](https://doi.org/10.1088/1538-3873/aae476)
- Jiang, Y.-F., Stone, J. M., & Davis, S. W. 2014, *ApJ*, 796, 106, doi: [10.1088/0004-637X/796/2/106](https://doi.org/10.1088/0004-637X/796/2/106)
- Kakiichi, K., Egami, E., Fan, X., et al. 2024, *COSMOS-3D: A Legacy Spectroscopic/Imaging Survey of the Early Universe*, JWST Proposal. Cycle 3, ID. #5893
- Kelly, B. C., Bechtold, J., & Siemiginowska, A. 2009, *ApJ*, 698, 895, doi: [10.1088/0004-637X/698/1/895](https://doi.org/10.1088/0004-637X/698/1/895)
- Killi, M., Watson, D., Brammer, G., et al. 2023, arXiv e-prints, arXiv:2312.03065, doi: [10.48550/arXiv.2312.03065](https://doi.org/10.48550/arXiv.2312.03065)

- Kimura, Y., Yamada, T., Kokubo, M., et al. 2020, *ApJ*, 894, 24, doi: [10.3847/1538-4357/ab83f3](https://doi.org/10.3847/1538-4357/ab83f3)
- Klimek, E. S., Gaskell, C. M., & Hedrick, C. H. 2004, *ApJ*, 609, 69, doi: [10.1086/420809](https://doi.org/10.1086/420809)
- Kocevski, D. D., Hasinger, G., Brightman, M., et al. 2018, *ApJS*, 236, 48, doi: [10.3847/1538-4365/aab9b4](https://doi.org/10.3847/1538-4365/aab9b4)
- Kocevski, D. D., Finkelstein, S. L., Barro, G., et al. 2024, arXiv e-prints, arXiv:2404.03576, doi: [10.48550/arXiv.2404.03576](https://doi.org/10.48550/arXiv.2404.03576)
- Kokorev, V., Caputi, K. I., Greene, J. E., et al. 2024a, *ApJ*, 968, 38, doi: [10.3847/1538-4357/ad4265](https://doi.org/10.3847/1538-4357/ad4265)
- Kokorev, V., Chisholm, J., Endsley, R., et al. 2024b, arXiv e-prints, arXiv:2407.20320, doi: [10.48550/arXiv.2407.20320](https://doi.org/10.48550/arXiv.2407.20320)
- Kokubo, M., & Harikane, Y. 2024, arXiv e-prints, arXiv:2407.04777, doi: [10.48550/arXiv.2407.04777](https://doi.org/10.48550/arXiv.2407.04777)
- Koposov, S., Speagle, J., Barbary, K., et al. 2024, joshspeagle/dynesty: v2.1.4, v2.1.4, Zenodo, doi: [10.5281/zenodo.12537467](https://doi.org/10.5281/zenodo.12537467)
- Kozłowski, S., Kochanek, C. S., Udalski, A., et al. 2010, *ApJ*, 708, 927, doi: [10.1088/0004-637X/708/2/927](https://doi.org/10.1088/0004-637X/708/2/927)
- Labbé, I., van Dokkum, P., Nelson, E., et al. 2023, *Nature*, 616, 266, doi: [10.1038/s41586-023-05786-2](https://doi.org/10.1038/s41586-023-05786-2)
- Labbe, I., Greene, J. E., Bezanson, R., et al. 2023, arXiv e-prints, arXiv:2306.07320, doi: [10.48550/arXiv.2306.07320](https://doi.org/10.48550/arXiv.2306.07320)
- Lanzuisi, G., Delvecchio, I., Berta, S., et al. 2017, *A&A*, 602, A123, doi: [10.1051/0004-6361/201629955](https://doi.org/10.1051/0004-6361/201629955)
- Larson, R. L., Finkelstein, S. L., Kocevski, D. D., et al. 2023, *ApJL*, 953, L29, doi: [10.3847/2041-8213/ace619](https://doi.org/10.3847/2041-8213/ace619)
- Leung, G. C. K., Bagley, M. B., Finkelstein, S. L., et al. 2023, *ApJL*, 954, L46, doi: [10.3847/2041-8213/acf365](https://doi.org/10.3847/2041-8213/acf365)
- Li, Z., Inayoshi, K., Chen, K., Ichikawa, K., & Ho, L. C. 2024, arXiv e-prints, arXiv:2407.10760, doi: [10.48550/arXiv.2407.10760](https://doi.org/10.48550/arXiv.2407.10760)
- Lyu, J., Alberts, S., Rieke, G. H., & Rujopakarn, W. 2022, *ApJ*, 941, 191, doi: [10.3847/1538-4357/ac9e5d](https://doi.org/10.3847/1538-4357/ac9e5d)
- Lyu, J., Alberts, S., Rieke, G. H., et al. 2024, *ApJ*, 966, 229, doi: [10.3847/1538-4357/ad3643](https://doi.org/10.3847/1538-4357/ad3643)
- Ma, Y., Greene, J. E., Setton, D. J., et al. 2024, arXiv e-prints, arXiv:2410.06257, doi: [10.48550/arXiv.2410.06257](https://doi.org/10.48550/arXiv.2410.06257)
- MacLeod, C. L., Ivezić, Ž., Kochanek, C. S., et al. 2010, *ApJ*, 721, 1014, doi: [10.1088/0004-637X/721/2/1014](https://doi.org/10.1088/0004-637X/721/2/1014)
- MacLeod, C. L., Brooks, K., Ivezić, Ž., et al. 2011, *ApJ*, 728, 26, doi: [10.1088/0004-637X/728/1/26](https://doi.org/10.1088/0004-637X/728/1/26)
- Madau, P., & Haardt, F. 2024, arXiv e-prints, arXiv:2410.00417, doi: [10.48550/arXiv.2410.00417](https://doi.org/10.48550/arXiv.2410.00417)
- Maiolino, R., Scholtz, J., Curtis-Lake, E., et al. 2023, arXiv e-prints, arXiv:2308.01230, doi: [10.48550/arXiv.2308.01230](https://doi.org/10.48550/arXiv.2308.01230)
- Maiolino, R., Risaliti, G., Signorini, M., et al. 2024, arXiv e-prints, arXiv:2405.00504, doi: [10.48550/arXiv.2405.00504](https://doi.org/10.48550/arXiv.2405.00504)
- Marchesi, S., Civano, F., Elvis, M., et al. 2016, *ApJ*, 817, 34, doi: [10.3847/0004-637X/817/1/34](https://doi.org/10.3847/0004-637X/817/1/34)
- Matthee, J., Naidu, R. P., Brammer, G., et al. 2024, *ApJ*, 963, 129, doi: [10.3847/1538-4357/ad2345](https://doi.org/10.3847/1538-4357/ad2345)
- Nardiello, D., Bedin, L. R., Burgasser, A., et al. 2022, *MNRAS*, 517, 484, doi: [10.1093/mnras/stac2659](https://doi.org/10.1093/mnras/stac2659)
- O'Brien, R., Jansen, R. A., Grogan, N. A., et al. 2024, *ApJS*, 272, 19, doi: [10.3847/1538-4365/ad3948](https://doi.org/10.3847/1538-4365/ad3948)
- Oesch, P. A., Brammer, G., Naidu, R. P., et al. 2023, *MNRAS*, 525, 2864, doi: [10.1093/mnras/stad2411](https://doi.org/10.1093/mnras/stad2411)
- Pacucci, F., & Narayan, R. 2024, arXiv e-prints, arXiv:2407.15915, doi: [10.48550/arXiv.2407.15915](https://doi.org/10.48550/arXiv.2407.15915)
- Pérez-González, P. G., Barro, G., Rieke, G. H., et al. 2024, *ApJ*, 968, 4, doi: [10.3847/1538-4357/ad38bb](https://doi.org/10.3847/1538-4357/ad38bb)
- Perrin, M. D., Sivaramakrishnan, A., Lajoie, C.-P., et al. 2014, in *Society of Photo-Optical Instrumentation Engineers (SPIE) Conference Series*, Vol. 9143, *Space Telescopes and Instrumentation 2014: Optical, Infrared, and Millimeter Wave*, ed. J. Oschmann, Jacobus M., M. Clampin, G. G. Fazio, & H. A. MacEwen, 91433X, doi: [10.1117/12.2056689](https://doi.org/10.1117/12.2056689)
- Planck Collaboration, Aghanim, N., Akrami, Y., et al. 2020, *A&A*, 641, A6, doi: [10.1051/0004-6361/201833910](https://doi.org/10.1051/0004-6361/201833910)
- Radcliffe, J. F., Garrett, M. A., Muxlow, T. W. B., et al. 2018, *A&A*, 619, A48, doi: [10.1051/0004-6361/201833399](https://doi.org/10.1051/0004-6361/201833399)
- Reines, A. E., & Volonteri, M. 2015, *ApJ*, 813, 82, doi: [10.1088/0004-637X/813/2/82](https://doi.org/10.1088/0004-637X/813/2/82)
- Rieke, G., Alberts, S., Shivaee, I., et al. 2024, arXiv e-prints, arXiv:2406.03518, doi: [10.48550/arXiv.2406.03518](https://doi.org/10.48550/arXiv.2406.03518)
- Rigby, J., Perrin, M., McElwain, M., et al. 2023, *PASP*, 135, 048001, doi: [10.1088/1538-3873/acb293](https://doi.org/10.1088/1538-3873/acb293)
- Sadowski, A. 2009, *ApJS*, 183, 171, doi: [10.1088/0067-0049/183/2/171](https://doi.org/10.1088/0067-0049/183/2/171)
- Sesar, B., Ivezić, Ž., Lupton, R. H., et al. 2007, *AJ*, 134, 2236, doi: [10.1086/521819](https://doi.org/10.1086/521819)
- Shen, Y., Zhuang, M.-Y., Li, J., et al. 2024, arXiv e-prints, arXiv:2408.12713, doi: [10.48550/arXiv.2408.12713](https://doi.org/10.48550/arXiv.2408.12713)
- Speagle, J. S. 2020, *MNRAS*, 493, 3132, doi: [10.1093/mnras/staa278](https://doi.org/10.1093/mnras/staa278)
- Taylor, M. B. 2005, in *Astronomical Society of the Pacific Conference Series*, Vol. 347, *Astronomical Data Analysis Software and Systems XIV*, ed. P. Shopbell, M. Britton, & R. Ebert, 29

- Ulrich, M.-H., Maraschi, L., & Urry, C. M. 1997, *ARA&A*, 35, 445, doi: [10.1146/annurev.astro.35.1.445](https://doi.org/10.1146/annurev.astro.35.1.445)
- Vanden Berk, D. E., Wilhite, B. C., Kron, R. G., et al. 2004, *ApJ*, 601, 692, doi: [10.1086/380563](https://doi.org/10.1086/380563)
- Vanderplas, J., Connolly, A., Ivezić, Ž., & Gray, A. 2012, in *Conference on Intelligent Data Understanding (CIDU)*, 47–54, doi: [10.1109/CIDU.2012.6382200](https://doi.org/10.1109/CIDU.2012.6382200)
- Wang, B., de Graaff, A., Davies, R. L., et al. 2024a, arXiv e-prints, arXiv:2403.02304, doi: [10.48550/arXiv.2403.02304](https://doi.org/10.48550/arXiv.2403.02304)
- Wang, B., Leja, J., de Graaff, A., et al. 2024b, *ApJL*, 969, L13, doi: [10.3847/2041-8213/ad55f7](https://doi.org/10.3847/2041-8213/ad55f7)
- Watarai, K.-y., Fukue, J., Takeuchi, M., & Mineshige, S. 2000, *PASJ*, 52, 133, doi: [10.1093/pasj/52.1.133](https://doi.org/10.1093/pasj/52.1.133)
- Weaver, J. R., Cutler, S. E., Pan, R., et al. 2024, *ApJS*, 270, 7, doi: [10.3847/1538-4365/ad07e0](https://doi.org/10.3847/1538-4365/ad07e0)
- Williams, C. C., Tacchella, S., Maseda, M. V., et al. 2023, *ApJS*, 268, 64, doi: [10.3847/1538-4365/acf130](https://doi.org/10.3847/1538-4365/acf130)
- Williams, C. C., Alberts, S., Ji, Z., et al. 2024, *ApJ*, 968, 34, doi: [10.3847/1538-4357/ad3f17](https://doi.org/10.3847/1538-4357/ad3f17)
- Xue, Y. Q., Luo, B., Brandt, W. N., et al. 2016, *ApJS*, 224, 15, doi: [10.3847/0067-0049/224/2/15](https://doi.org/10.3847/0067-0049/224/2/15)
- Yan, H., Ma, Z., Sun, B., et al. 2023, *ApJS*, 269, 43, doi: [10.3847/1538-4365/ad0298](https://doi.org/10.3847/1538-4365/ad0298)
- Yang, G., Papovich, C., Bagley, M. B., et al. 2023, *ApJL*, 956, L12, doi: [10.3847/2041-8213/acfaa0](https://doi.org/10.3847/2041-8213/acfaa0)
- Yue, M., Eilers, A.-C., Ananna, T. T., et al. 2024, arXiv e-prints, arXiv:2404.13290, doi: [10.48550/arXiv.2404.13290](https://doi.org/10.48550/arXiv.2404.13290)
- Zhuang, M.-Y., & Shen, Y. 2024, *ApJ*, 962, 139, doi: [10.3847/1538-4357/ad1183](https://doi.org/10.3847/1538-4357/ad1183)
- Zu, Y., Kochanek, C. S., & Peterson, B. M. 2011, *ApJ*, 735, 80, doi: [10.1088/0004-637X/735/2/80](https://doi.org/10.1088/0004-637X/735/2/80)
- Zuo, W., Wu, X.-B., Liu, Y.-Q., & Jiao, C.-L. 2012, *ApJ*, 758, 104, doi: [10.1088/0004-637X/758/2/104](https://doi.org/10.1088/0004-637X/758/2/104)